^{238}U–^{230}Th–^{226}Ra Disequilibria Constraints on the Magmatic Evolution of the Cumbre Vieja Volcanics on La Palma, Canary Islands

S. Turner[1]*, K. Hoernle[2,3], F. Hauff[2], T. S. Johansen[4], A. Klügel[5], T. Kokfelt[6] and C. Lundstrom[7]

[1]Department of Earth and Planetary Sciences, Macquarie University, Sydney, NSW 2109, Australia; [2]GEOMAR Helmholtz Centre for Ocean Research Kiel, Wischhofstrasse 1–3, D-24148 Kiel, Germany; [3]Christian-Albrechts University, D-24118 Kiel, Germany; [4]Agder Natural Museum, Gimle Vei 23, 4630 Kristiansand, Norway; [5]Universität Bremen, Fachbereich Geowissenschaften, Postfach 330440, D-28334, Bremen, Germany; [6]National Geological Survey of Denmark and Greenland, 1350 Copenhagen K, Denmark and [7]Department of Geology, University of Illinois at Urbana Champaign, Champaign, IL 61801, USA

*Corresponding author. Telephone: (61) 2 9850 8363. Fax: (61) 2 9850 6904. E-mail: simon.turner@mq.edu.au

ABSTRACT

A suite of 48 samples, including both historical and prehistoric lavas and some plutonic rocks, have been analysed from the Cumbre Vieja rift, La Palma, Canary Islands. Additionally, mineral–melt partition coefficients have been measured for clinopyroxene, plagioclase, amphibole, titanite and apatite in selected rocks. The lavas range from basanite to phonolite ($SiO_2 = 41\cdot2$–$57\cdot5$ wt % and $MgO = 10$–$0\cdot8$ wt %) in composition and form coherent, curvilinear major and trace element arrays in variation diagrams, irrespective of eruption age. The mafic lavas have typical ocean island incompatible trace element patterns and Sr, Nd and Pb isotope compositions show little variation but have a HIMU-type character. Generation of the parental magmas is inferred to have involved ~4% dynamic melting of a garnet lherzolite source that may have previously been metasomatized by melts derived from a recycled mafic component containing residual phlogopite. The major process of differentiation to phonotephrite involved fractional crystallization of basanitic magmas that evolved along the same liquid line of descent under similar pressure–temperature conditions. Numerical simulations using the MELTS algorithm suggest that this occurred across a temperature interval from *c.* 1320 to 950°C at 400 MPa and an oxygen fugacity equivalent to quartz–fayalite–magnetite (QFM), with an initial H_2O content of $0\cdot3$ wt %. The later stages of differentiation (<5 wt % MgO) were dominated by mixing with partial melts of young syenites formed from earlier magma batches. All of the lavas are characterized by ^{230}Th and ^{226}Ra excesses and (^{230}Th/^{238}U) decreases with decreasing Nb/U and increasing SiO_2, with no accompanying change in (^{226}Ra/^{230}Th). To explain the observations, we propose a model in which there was a significant role for amphibole, and more importantly accessory titanite, in decre'asing Nb/U, Ce/Pb and Th/U ratios and increasing or buffering (^{226}Ra/^{230}Th) ratios during the later stages of differentiation and magma mixing. These processes all occurred over a few millennia in small magma batches that were repeatedly emplaced within the mid-crust of the Cumbre Vieja rift system prior to rapid transport to the surface.

Key words: La Palma; ocean island basalt evolution; magmatic timescales; titanite fractionation

INTRODUCTION

Lavas erupted on ocean islands offer an opportunity to explore magma evolution away from the possible complicating effects of contamination by continental lithosphere. They typically have alkaline affinity and some ocean islands erupt a continuum of compositions ranging from basanite to phonolite. In addition to traditional geochemical investigations, the timescale information afforded by U-series isotope data can place important constraints on the physical mechanisms involved in magmatic evolution (Dosseto et al., 2010). Recent studies have shown that mantle melting rates beneath mid-ocean ridges and ocean islands are likely to be controlled by a combination of variable upwelling rates and the possible presence of mafic lithologies that commence melting deeper and at faster rates than peridotite (e.g. Kokfelt et al., 2003; Bourdon et al., 2005; Koornneef et al., 2012; Elkins et al., 2014; Turner et al., 2015). After segregation from the mantle, primitive melts probably ascend by channelled flow at rates that are too fast to be recorded by ^{230}Th or ^{226}Ra (e.g. Turner et al., 2001; Stracke et al., 2006; Turner & Bourdon, 2010). If correct, the ^{226}Ra data can then be used to gain insights into the porosity of the melting region. However, such melts may become modified by interaction with fusible components in the lithosphere (e.g. Claude-Ivanaj et al., 1998; Lundstrom et al., 2003) and disequilibria can decay during subsequent magma storage and evolution in the crust. In the simplest case of crystallization in response to cooling, small and shallow magma systems are likely to promote rapid differentiation (e.g. Blake & Rogers, 2005; Turner et al., 2010) whereas deep or large systems will evolve more slowly (e.g. Annen et al., 2006; Dosseto et al., 2008). Moreover, the effects of assimilation can promote faster differentiation than might occur under closed-system situations (George et al., 2004). To assess some of these processes further we undertook a full geochemical and U-series investigation of young lavas from La Palma at the western end of the Canary Islands archipelago to complement an earlier study of Lanzarote at the eastern end (Thomas et al., 1999). We combine our new results with previously published data to explore the timescales of magma evolution beneath this island.

GEOLOGICAL BACKGROUND AND SAMPLE SELECTION

The shallow bathymetry of the Canary Islands archipelago relative to the age of the plate (150–175 Ma) is inferred to reflect the impingement of a mantle plume on the base of the lithosphere. Geophysical data indicate that this plume has a low buoyancy flux of $\sim$1 Mg s^{-1} (Sleep, 1990). La Palma lies at the western end of the island chain and is volcanically active (Fig. 1). It consists of three main volcanic units, as described in detail by Middlemost (1972), Ancochea et al. (1994) and Carracedo et al. (2001): a 4–2 Ma basal complex, a

1·7–0·4 Ma older volcanic series, and a <123 kyr volcanic series that includes seven historical eruptions (see below). As shown in Fig. 1, all of the recent eruptions are confined to Cumbre Vieja, a north–south-trending rift zone in the southern half of the island (Middlemost, 1972). Lava compositions range from basanite to phonolite.

The petrography of the lavas is illustrated in Fig. 2. The petrography of samples from the 1949 and 1585 eruptions has been described in detail by Klügel et al. (2000, 2005) and Johansen et al. (2005), respectively. The basanites and tephrites occasionally contain xenoliths of pyroxenite, gabbro, amphibole cumulate and phonolite (e.g. Klügel et al., 2000; Johansen et al., 2005). In general, the basanites contain 5–20% phenocrysts of titaniferous augite and olivine in subequal amounts, along with minor Ti-magnetite, set in a glassy matrix containing abundant plagioclase, clinopyroxene, olivine, and Fe–Ti oxide microlites. The tephrites contain phenocrysts of kaersutitic amphibole, clinopyroxene, Ti-magnetite and rare olivine in a groundmass of glass, plagioclase, clinopyroxene and Fe–Ti oxides. Phonotephrites and tephriphonolites contain phenocrysts of kaersutitic amphibole, plagioclase, clinopyroxene, haüyne, titanite, opaque oxides and minor apatite. The phonolites contain phenocrysts of plagioclase (10%), kaersutitic amphibole (2%), clinopyroxene (3%), haüyne, titanite, and minor apatite and Fe–Ti oxide. Glomerocrystic aggregates are common in all of the rock types.

The mineral chemistry has been documented and interpreted by Klügel et al. (2000) and we have not undertaken further appraisal as part of the present study. Previous studies inferred crystallization temperatures of 1220–1110°C and redox conditions slightly above the quartz–fayalite–magnetite (QFM) buffer (Klügel et al., 2000). Thermobarometry and fluid inclusion studies suggest that the Cumbre Vieja magmas differentiated and ponded at two successive pressures (410–770 and 240–470 MPa) corresponding to $\sim$20 km depth within the lithospheric mantle and $\sim$13 km near the base of the oceanic crust (Klügel et al., 2000, 2005). Based on phenocryst zonation and the presence of amphibole breakdown rims in the tephrites, Klügel et al. (1997, 2000) argued for melt ascent from the mantle magma storage reservoirs to the surface within hours to days.

Geochemical data indicate that the primary Cumbre Vieja magmas are similar to those erupted on Lanzarote and were generated by small (1–5%) degrees of partial melting within the garnet stability field (Elliott, 1991; Thomas et al., 1999). Magmatic evolution has been suggested to occur via crystal fractionation combined with mixing between discrete magma batches, as indicated by major element modelling and reversely zoned phenocrysts (Klügel et al., 2000; Praegel & Holm, 2006). Radiogenic isotope data indicate a HIMU-type mantle source composition (Elliott, 1991; Hoernle et al., 1991), which has been inferred potentially to contain up to 10% of recycled pyroxenite or eclogite (Praegel & Holm,
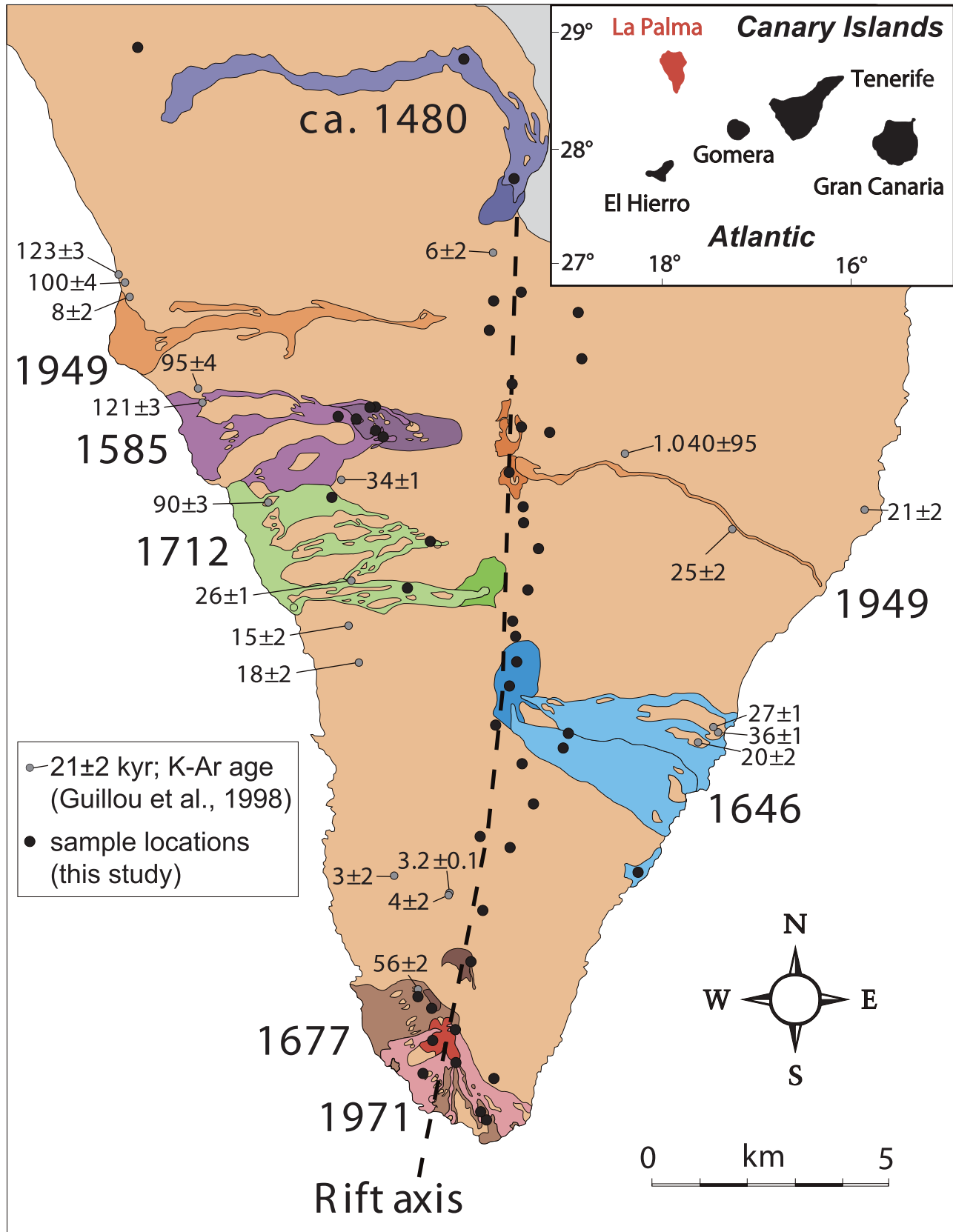
Fig. 1. Map of the Cumbre Vieja rift on La Palma showing the sample locations of this study [modified after Carracedo *et al.* (1999)]. Coloured areas represent historical eruptions; grey circles are locations where eruption ages were obtained by the K–Ar unspiked method (Guillou *et al.*, 1998).
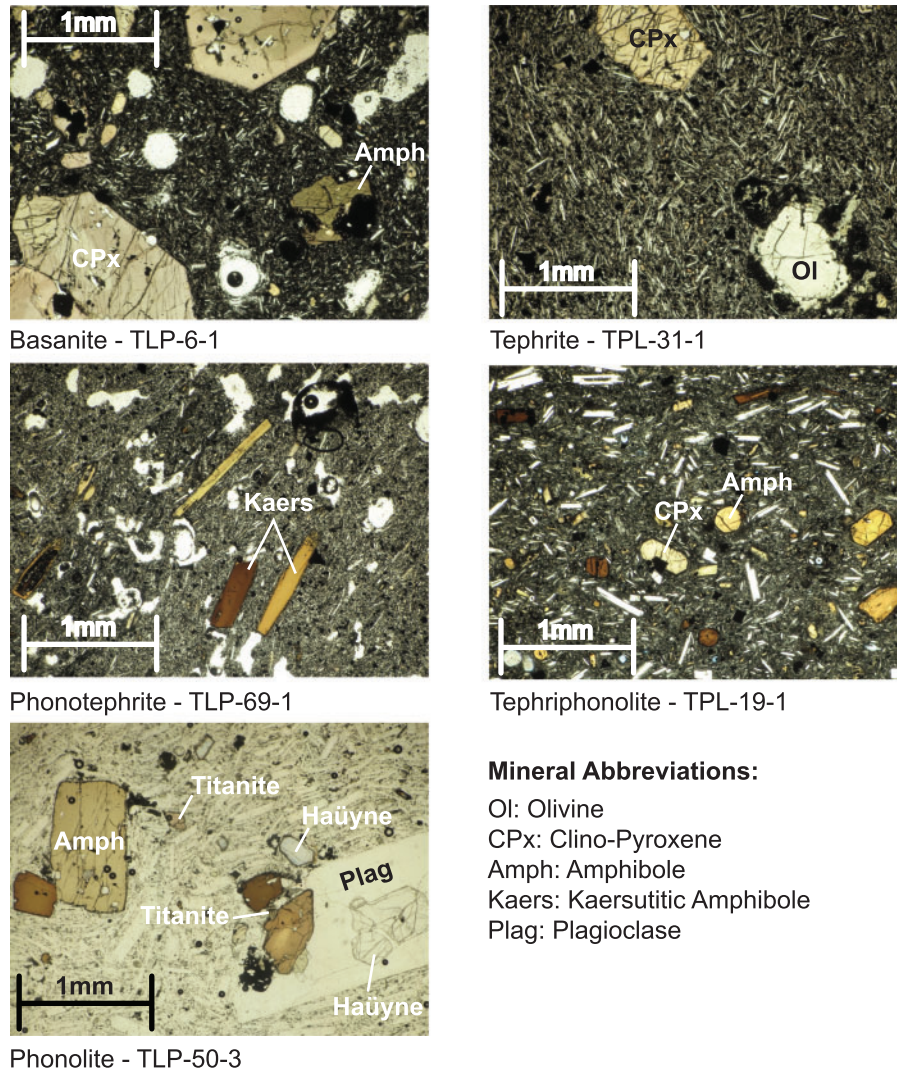
Fig. 2. Plane-polarized light photomicrographs of a representative basanite, tephrite, phonotephrite, tephriphonolite and phonolite from Cumbre Vieja. The phonolite includes a small fragment of a haüyne–amphibole gabbro xenolith (lower right corner); such xenoliths are commonly found in Cumbre Vieja lavas.

2006; Day *et al.*, 2010). Previously published U-series data from the other Canary Islands have been used to constrain mantle melting processes, lithospheric interaction and differentiation timescales (Sigmarsson *et al.*, 1992; Thomas *et al.*, 1999; Lundstrom *et al.*, 2003). For La Palma, Johansen *et al.* (2005) used U-series data from the products of the AD 1585 eruption to infer that differentiation from basanite to phonolite occurred within 1550–1750 years.

We selected 19 samples from the 1971, 1949, 1712, 1677, 1646 and AD 1480 eruptions and 29 samples from prehistoric lava flows as well as four intrusive rocks representing possible crustal contaminants, for major and trace element analysis (Tables 1–3). From these, a subset of 12 samples was selected for Sr–Nd–Pb isotope analysis (Table 4). Tables 3 and 4 also include some previously published data (identified by italics) from Klügel *et al.* (2000) and Johansen *et al.* (2005). We also chose 21 samples for U-series isotope analysis, including

13 prehistoric samples (Table 5). Ra isotope data were obtained on 11 of the historical samples and seven of the prehistoric samples, the latter to ascertain whether or not their Th isotope ratios could have been modified by post-eruptive decay.

To permit quantitative trace element modelling, mineral–melt partition coefficients were measured for clinopyroxene, plagioclase, amphibole, titanite and apatite in rocks selected to encompass the full compositional array of the suite. These data should also be of use in studies of other suites of ocean island alkaline volcanic rocks.

ANALYTICAL TECHNIQUES

Fresh hand specimens free of any signs of weathering were crushed in a steel jaw crusher. Sample chips were then repeatedly washed with deionized water in an ultrasonic bath until a clear solution was obtained.

Table 1: Sample descriptions, locations and map coordinates for La Palma samples

Sample no.	Rock type and description	Locality	metres a.s.l.	Coordinates
1971 eruption				
TLP 31-1	Tephrite flow	At contact with 1677 flow, by road	120	221704/3151311
TLP 78-1	Basanite flow	From vent just underneath V. de Teneguia, north side	368	221201/3152954
TLP 79-1	Basanite, block of aa lava	SW flank of V. de Teneguia, upper part of flow	327	220627/3152640
TLP 81-1	Basanite, block of aa lava	Seaside road, at the end of the same flow as TLP 79/80	49	220470/3151928
TLP 85-1	Basanite, block of aa lava	Same flow as TLP 82-1, SE of V. de Teneguia	307	221162/3152275
1712 eruption				
TLP 6-1	Basanite or tephrite	Same flow as 5-1, lowermost sequence	1263	220895/3162749
TLP 6-6	Basanite	Same flow as 5-1, uppermost sequence	1268	220895/3162749
TLP 98-1	Basanite, aa flow	Northernmost 1712 flow close to north flank, by foot trail	569	218705/3163693
TLP 111-1	Basanite flow, 1 m thick, uppermost unit	About halfway between P.I.R.S. and main road, south side of road	921	220118/3161870
1677 eruption				
TLP 25-3	Gabbro xenolith	East flank of V. de San Antonio	648	221447/3154102
TLP 30-1	Basanite flow	Near intersection with road towards Faro de Fuencaliente	91	221724/3151120
TLP 30-2	Amphibole-pyroxenite cumulate xenolith	From same flow as TLP 30-1	91	221724/3151120
TLP 77-1	Basanite flow, pahoehoe, uppermost sequence	Midway between V. San Antonio and Teneguia, by road	457	220841/3153338
1646 eruption				
TLP 40-1	Basanite bomb	Rim of the 2nd crater of the S. Martin system	1572	222334/3160250
TLP 43-1	Basanite bomb	Southernmost crater of the S. Martin system	1494	222185/3159651
TLP 76-1	Basanite flow, pahoehoe	Flank eruption near El Puertito	100	224927/3156120
TLP 119-1	Basanite flow, 1 m thick	At roadcut, 80 m further north from previous location	1121	223186/3158481
1480 eruption				
TLP 58-1	Basanite, pahoehoe	Central part of 1480 flow, close to vent	1151	222457/3170142
TLP 62-1	Basanite, aa block	Central part of 1480 flow, relatively near Mña Colorada	883	221358/3172610
Prehistoric lavas				
TLP 9-1	Tephrite flow	SE of Mña de los Pérez	1050	221663/3157050
TLP 10-1	Phonolite plug	By rocky road NE of Mña del Pino	1059	222891/3157472
TLP 13-1	Phonotephrite bomb	West flank of Birigoyo, on 'volcano trail'	1632	222136/3167609
TLP 15-1	Basanite flow	Mña La Barquita, by 'volcano trail'	1618	221906/3167044
TLP 17-1	Basanite bomb	NE of Los Charcos	1767	222293/3165952
TLP 18-2	Tephrite bomb, older than AD 1949	Hoyo Negro crater, buried in soil	1869	222623/3164982
TLP 19-2	Tephriphonolite, spatter	Near eruptive vent at Nambroque	1907	222969/3164911
TLP 21-1A-S	MORB-type gabbro xenoliths, 19 samples	Northern rim of Duraznero crater	1850	222466/3164302
TLP 22-1	Basanite bomb	Crater slightly south of Duraznero	1882	222419/3163635
TLP 23-1	Basanite bomb	Deseada ll, 100 m south of peak	1925	222424/3163346
TLP 27-1	Phonolite dome	SW of V. de San Antonio, below road	427	220534/3153682
TLP 32-1A	Basanite, spatter	Cinder cone, uppermost black layer	195	221944/3151992
TLP 32-1B	Basanite, spatter	Cinder cone, yellow layer underneath the black layer	195	221944/3151992
TLP 34-1	Tephrite bomb	East of Mña Negra	1830	222766/3162589
TLP 36-1	Basanite bomb	West of Cabrito	1761	222524/3161886
TLP 37-1	Basanite, spatter	North of Mña Cabrera	1643	222344/3161120
TLP 38-1	Basanite bomb	Mña Cabrera	1630	222344/3160720
TLP 44-1	Basanite bomb	Mña Pelada	1390	222035/3159197
TLP 46-1	Phonotephrite flow	Volcan Fuego	1227	222690/3158066
TLP 64-1	Basanite bomb	Crater just NE of Birigoyo	1647	222713/3167712
TLP 69-1	Tephrite bomb	Vent NW of Mña El Caldero	1596	223312/3167192
TLP 70-1	Basanite bomb	Peak of Mña El Caldero	1635	223681/3166722
TLP 108-1	Tephrite bomb, overlain by 20–30 m thick tephra layer	Mña de Triana, north side of horseshoe-shaped cone	311	214747/3172626
TLP 116-1	Tephrite bomb	Mña del Pino, near TV antenna, by dirt road	1000	222250/3156839
TLP 126-1	Tephrite bomb	Mña los Riveros, near peak	853	221607/3155597
Volcan de Taburiente				
TLP 52-9	Diorite boulder	Barranco Las Angustias	∼360	217246/3177769
TLP 52-10	Diorite or granodiorite boulder	Barranco Las Angustias	∼360	217246/3177769
TLP 52-12	Syenite cobble	Barranco Las Angustias	∼360	217246/3177769
TLP 52-14	Syenite cobble	Barranco Las Angustias	∼360	217246/3177769

Table 2: XRF major element (normalized to 100% anhydrous) and ICP-MS trace element data* for La Palma lavas

| Sample: | TLP 78-1 | TLP 79-1 | TLP 81-1 | TLP 85-1 | TLP 31-1 | KLA 1-5-08 | KLA1-2-10* |
Age:	AD 1971	AD 1971	AD 1971	AD 1971	AD 1971	AD 1949	AD 1949
SiO_2	43·15	43·30	43·07	42·88	44·96	44·11	44·21
TiO_2	3·74	3·62	3·74	3·76	3·51	3·48	3·40
Al_2O_3	14·00	14·05	14·34	13·91	16·04	13·90	13·92
FeO_{tot}	14·06	14·07	14·12	14·27	12·87	13·79	13·64
MnO	0·19	0·19	0·19	0·19	0·19	0·201	0·200
MgO	7·67	7·69	7·35	7·68	5·26	8·03	8·27
CaO	11·04	11·07	10·79	11·09	9·59	10·85	10·57
Na_2O	3·84	3·73	4·01	3·87	4·71	3·64	3·77
K_2O	1·45	1·42	1·49	1·43	1·88	1·31	1·33
P_2O_5	0·87	0·86	0·91	0·93	0·98	0·69	0·70
Rb	30·5	30·3	32·2	29·0	44·3	28·7	n.d.
Sr	1128	1033	1135	1113	1286	953	n.d.
Y	31·8	31·7	33·4	31·6	33·6	30·6	n.d.
Zr	333	304	317	323	410	314	n.d.
Nb	85	77	84	85	103	79	n.d.
Cs	0·363	0·342	0·357	0·357	0·517	0·335	n.d.
Ba	491	464	503	503	641	436	427·0
Ta	4·40	5·08	5·49	4·85	5·35	4·39	n.d.
Tl	0·00	0·09	0·10	0·00	0·00	0·00	n.d.
Pb	4·15	3·33	3·57	3·32	4·13	2·93	n.d.
Th	7·09	5·99	6·60	7·66	9·60	6·78	n.d.
U	1·89	1·79	1·89	2·00	2·51	1·77	n.d.
Sc	27·5	25·9	23·9	26·8	18·8	26·3	n.d.
V	353	313	304	357	296	326	276
Cr	220	231	202	212	35·4	328	325
Co	50	47·1	45·0	50·8	37·6	50·0	63·0
Ni	98	99	90	99	34	119	139
Cu	89	98	89	90	61	81	n.d.
Zn	126	111	109	128	133	119	121
Ga	22	22	23	22	24	21	n.d.
La	78	74	73	79	92	71	n.d.
Ce	154	153	157	157	175	140	n.d.
Pr	17·54	17·29	17·67	18·13	19·60	15·89	n.d.
Nd	70	69	74	74	76	62	n.d.
Sm	12·76	12·47	13·63	13·69	13·64	11·45	n.d.
Eu	3·73	3·90	3·96	3·96	3·98	3·42	n.d.
Gd	10·93	10·64	10·84	11·48	11·26	9·76	n.d.
Tb	1·37	1·37	1·40	1·43	1·47	1·26	n.d.
Dy	7·59	7·29	7·50	7·69	7·73	6·92	n.d.
Ho	1·28	1·27	1·32	1·36	1·35	1·23	n.d.
Er	3·19	3·21	3·46	3·22	3·39	2·91	n.d.
Tm	0·410	0·411	0·466	0·401	0·429	0·388	n.d.
Yb	2·23	2·31	2·55	2·43	2·52	2·20	n.d.
Lu	0·316	0·293	0·328	0·324	0·362	0·321	n.d.
Hf	7·43	6·72	6·85	7·98	8·74	7·27	n.d.

(continued)

Following drying overnight sample chips were selected under a binocular microscope for powder preparation using an agate mortar and swing mill. A split of 0·5–2 mm sized chips was put aside for Sr–Nd–Pb chemistry. The analytical techniques outlined below have been described in detail by Kokfelt *et al.* (2003, 2006). Major element and selected trace element concentrations were determined on fused beads using a Philips PW1480 X-ray fluorescence spectrometer at GEOMAR. Over the course of the study standard materials JB-2 and JB-3 were repeatedly analysed (*n* = 5) along with the samples and these results are reported in Supplementary Data (SD) Electronic Appendix 1 (supplementary data are available for downloading at http://www.petrology.oxfordjournals.org). Relative standard deviation (RSD) is well below 0·1% for all oxides except

SiO_2 (≤0·2%). Accuracy relative to the values of Imai *et al.* (1995) is generally better than 2%, except for a 5% deviation for MgO in JB-2.

Trace element concentrations were measured by inductively coupled plasma mass spectrometry (ICP-MS) on a ThermoFinnigan Element2 at the Institute of Geosciences, University of Bremen, following the procedures outlined by Garbe-Schönberg 1993, Schwarz *et al.* (2005). Results of repeat digests of USGS reference material BCR-2 (*n* = 11), BIR-1 (*n* = 2) and BHVO-2 (*n* = 3) and comparison with preferred values from the GeoReM database (Jochum *et al.*, 2005) are provided in SD Data Electronic Appendix 2. Reproducibility is better than 10%, except for Sc, Ni, Rb, Y, Eu, Lu, Hf, Tl, Pb, Th and U (10–17·5%) in BCR-2 and for Hf, Tl and Pb (11–21%) in BIR-1 and BHVO-2. Accuracy for BCR-2 and BHVO-2 is better

Table 2: Continued

Sample: Age:	KLA1-5-07 AD 1949	KLA1-2-15 AD 1949	KLA1-5-19 AD 1949	TLP 6-6 AD 1712	TLP 98-1 AD 1712	TLP 111-1 AD 1712	TLP 6-1 AD 1712
SiO_2	44·00	45·73	45·70	42·93	43·09	42·86	43·28
TiO_2	3·51	3·39	3·43	3·67	3·71	3·72	3·76
Al_2O_3	13·82	16·22	16·22	13·31	13·44	13·32	14·93
FeO_{tot}	13·80	11·61	11·77	13·65	13·63	13·84	13·36
MnO	0·202	0·213	0·213	0·19	0·19	0·19	0·20
MgO	8·08	4·95	4·96	8·39	8·12	8·22	6·08
CaO	10·77	9·10	9·19	11·52	11·53	11·60	10·76
Na_2O	3·81	5·51	5·30	3·74	3·66	3·71	4·42
K_2O	1·28	2·38	2·34	1·67	1·69	1·63	2·05
P_2O_5	0·73	0·90	0·88	0·93	0·93	0·92	1·17
Rb	33·51	68·91	67·77	40·4	41·2	39·2	52
Sr	1150	1704	1694	1215	1255	1166	1553
Y	38·1	44·4	44·1	34·0	33·4	32·6	39·5
Zr	331	515	512	325	343	307	416
Nb	78	129	127	97	103	92	126
Cs	0·38	0·79	0·77	0·454	0·489	0·442	0·613
Ba	452	794	786	596	630	583	785
Ta	4·10	6·19	6·19	6·09	5·49	6·20	6·72
Tl	0·04	0·07	0·06	0·13	0·00	0·11	0·00
Pb	3·90	6·15	5·82	4·04	3·83	4·34	4·75
Th	6·45	12·56	12·62	8·01	10·18	7·87	13·03
U	1·73	3·54	3·49	2·22	2·59	2·21	3·42
Sc	20	8	11	27·5	27·5	26·4	21·5
V	298	237	257	343	354	312	356
Cr	309	46	47	349	329	343	84
Co	61	28	34	51·0	49·5	46·2	42·6
Ni	133	46	50	121	110	107	52
Cu	n.d.	n.d.	n.d.	101	90	96	72
Zn	127	129	130	114	122	110	132
Ga	28	31	31	22	21	21	23
La	67	109	109	89	97	88	130
Ce	131	201	201	167	185	175	241
Pr	15·60	22·22	22·22	18·76	20·5	19·02	26·0
Nd	60	81	81	69	80	74	98
Sm	11·33	14·18	13·87	12·80	14·11	13·84	16·99
Eu	3·41	4·08	4·09	3·81	4·13	4·03	4·76
Gd	9·92	11·86	11·97	10·74	11·53	11·07	13·32
Tb	1·33	1·53	1·53	1·42	1·46	1·46	1·72
Dy	6·74	7·55	7·62	7·25	7·99	7·83	9·12
Ho	1·19	1·34	1·37	1·27	1·39	1·32	1·58
Er	2·98	3·48	3·51	3·24	3·25	3·41	3·72
Tm	0·36	0·44	0·44	0·422	0·432	0·469	0·477
Yb	2·22	2·71	2·70	2·39	2·47	2·53	2·85
Lu	0·31	0·38	0·37	0·295	0·354	0·334	0·408
Hf	6·79	9·14	9·34	6·48	8·19	7·21	9·10

(continued)

than 7%, except for Cr, Ni, Cu, Y, Ta and Th in BCR-2 and Cs, Ba, Ta, Tl, Pb, Th and U in BHVO-2.

The laser ICP-MS methods used for determining mineral–melt partition coefficients are given in the Appendix. Representative data for all the main mineral phases except olivine (for which the concentrations of most trace elements are too low for analysis) are given in Table 6 and the full results are provided in SD Electronic Appendix 3.

Sr, Nd and Pb isotope ratios were determined in static multi-collection mode by thermal ionization mass spectrometry (TIMS) on a Thermo Scientific TRITON (Sr–Nd) and a Finnigan MAT 262 RPQ^{2+} at GEOMAR. Chemical procedures followed those outlined by Jacques *et al.* (2013). Sr and Nd isotope ratios were normalized within run to $^{86}Sr/^{88}Sr = 0.1194$ and $^{146}Nd/^{144}Nd = 0.7219$,

respectively. Sample data are reported relative to $^{87}Sr/^{86}Sr = 0.710257 \pm 8$ ($n = 37$) for NBS987, $^{143}Nd/^{144}Nd = 0.511848 \pm 5$ ($n = 12$) for La Jolla and $^{143}Nd/^{144}Nd = 0.511712 \pm 6$ ($n = 20$) for our in-house Nd monitor SPEX. Because Pb isotopes were analyzed prior to the establishment of a Pb double-spike technique (Hoernle *et al.*, 2011) in our laboratory, the measured isotope ratios of the La Palma samples were externally mass bias corrected by normalizing the repeat measurements of NBS981 ($^{206}Pb/^{204}Pb = 16.900 \pm 7$, $^{207}Pb/^{204}Pb = 15.437 \pm 8$, $^{208}Pb/^{204}Pb = 36.527 \pm 27$, $n = 60$, 2003–2004) to our actual double spike (DS)-corrected NBS981 values ($^{206}Pb/^{204}Pb = 16.9417 \pm 27$, $^{207}Pb/^{204}Pb = 15.4991 \pm 27$, $^{208}Pb/^{204}Pb = 36.7250 \pm 70$, $n = 98$, 2012–2014). All above-mentioned errors are 2σ external and reported to the last significant digits.

Table 2: Continued

Sample:	TLP 25-1	TLP 30-1	TLP 77-1	TLP 11-1	TLP 40-1	TLP 43-1	TLP 76-1
Age:	AD 1677	AD 1677	AD 1677	AD 1646	AD 1646	AD 1646	AD 1646
SiO_2	43·48	43·21	43·29	42·91	42·93	42·92	42·87
TiO_2	3·61	3·65	3·70	3·71	3·69	3·63	3·71
Al_2O_3	13·71	13·57	13·61	13·20	13·18	12·97	13·47
FeO_{tot}	13·49	13·57	13·41	13·55	13·56	13·69	13·58
MnO	0·19	0·19	0·19	0·19	0·19	0·19	0·19
MgO	7·79	8·02	7·84	8·15	8·06	8·48	7·91
CaO	11·26	11·41	11·74	12·25	12·25	12·29	12·00
Na_2O	3·85	3·77	3·66	3·64	3·65	3·43	3·74
K_2O	1·75	1·70	1·67	1·54	1·59	1·54	1·60
P_2O_5	0·87	0·90	0·88	0·87	0·90	0·86	0·93
Rb	42·5	39·9	40·2	36·3	37·9	37·0	37·5
Sr	1267	1228	1276	1203	1276	1183	1216
Y	35·7	35·3	34·8	34·2	34·1	33·6	33·8
Zr	344	334	350	314	340	304	313
Nb	101	98	103	91	99	89	91
Cs	0·480	0·447	0·459	0·393	0·435	0·467	0·409
Ba	642	614	616	568	593	558	585
Ta	6·59	6·46	5·34	5·79	5·09	5·84	5·90
Tl	0·13	0·14	0·00	0·13	0·00	0·06	0·07
Pb	4·55	6·55	3·68	3·83	2·85	2·57	3·77
Th	9·55	9·18	9·06	8·34	10·05	8·42	8·80
U	2·56	2·36	2·30	2·22	2·48	2·23	2·35
Sc	25·2	26·0	29·0	30·0	30·4	30·0	27·3
V	331	319	362	352	372	343	332
Cr	305	322	297	336	318	365	297
Co	49·0	48·0	48·8	49·4	50	49·3	46·6
Ni	109	112	105	112	111	124	105
Cu	97	97	95	113	108	114	112
Zn	121	113	124	121	123	108	110
Ga	22	22	21	22	21	21	22
La	102	100	95	87	100	89	89
Ce	189	182	181	163	187	167	178
Pr	20·9	20·9	20·4	18·23	20·5	18·24	19·46
Nd	75	77	78	71	79	70	76
Sm	13·32	13·79	14·03	12·82	14·37	12·55	13·40
Eu	4·04	4·10	4·08	3·81	4·02	3·96	4·01
Gd	11·49	11·74	12·02	10·58	11·80	11·16	10·80
Tb	1·50	1·47	1·52	1·40	1·47	1·39	1·42
Dy	7·78	8·05	8·08	7·20	8·09	7·50	7·59
Ho	1·41	1·41	1·39	1·28	1·41	1·30	1·32
Er	3·46	3·52	3·41	3·31	3·36	3·25	3·45
Tm	0·463	0·452	0·430	0·444	0·423	0·448	0·480
Yb	2·51	2·55	2·49	2·31	2·34	2·29	2·44
Lu	0·321	0·336	0·356	0·305	0·340	0·306	0·322
Hf	7·32	7·23	7·90	6·62	7·66	6·56	6·92

(continued)

U, Th and Ra isotopes and concentrations were analysed by isotope dilution (ID)-TIMS using the Finnigan MAT 262 RPQ^{2+} system at GEOMAR, although some Ra analyses were also made at the University of Illinois at Urbana Champaign. Chemical separation and analysis methods have been described by Kokfelt *et al.* (2003). Analyses of the TML rock standard ($n = 12$) yielded Th $= 29·56 \pm 2·54$ ppm, U $= 10·62 \pm 0·90$ ppm, ^{226}Ra $= 3585 \pm 55$ fg g^{-1}, (^{234}U/^{238}U) $= 1·007 \pm 0·006$, (^{238}U/^{232}Th) $= 1·087 \pm 0·013$, (^{232}Th/^{230}Th) $= 1·090 \pm 0·004$ and (^{226}Ra/^{230}Th) $= 0·988 \pm 0·020$. Data for the rock standard AThO analysed at the same time as this study have been reported by Kokfelt *et al.* (2003). The data for both standards are within error of published data for these materials (Sims *et al.*, 2008). The ^{226}Ra data for the historical eruptions were corrected to eruptive values; no correction was applied to the Th isotopes.

RESULTS

The new whole-rock data are presented in Tables 2–5 and combined with published data for the AD 1585 eruption (Johansen *et al.*, 2005) in many of the subsequent diagrams. Overall, the lavas form highly coherent geochemical arrays, irrespective of eruption age. SiO_2 ranges from 41·2 to 57·5 wt %, across which range MgO decreases from 10 to 0·8 wt %. With a Mg# of 63 and Ni and Cr contents of 309 and 767 ppm, respectively, even the most primitive basanite (KLA 1-5-13) reported by Klügel *et al.* (2000) is significantly more evolved than a primary mantle melt. In Fig. 3 total alkalis range from 4·4 to 13·9 wt % and the corresponding lava classifications range from basanite to tephrite, phonotephrite, tephriphonolite and phonolites (Le Bas *et al.*, 1986). When plotted versus MgO, TiO_2, FeO_{tot} and CaO all decrease in concentration with decreasing MgO, whereas

Table 2: Continued

Sample:	TLP 119-1	TLP 58-1	TLP 62-1	TLP 15-1	TLP 17-1	TLP 22-1	TLP 23-1
Age:	AD 1646	AD 1480	AD 1480	prehistoric	prehistoric	prehistoric	prehistoric
SiO_2	43·12	43·89	43·47	43·67	43·99	41·21	41·49
TiO_2	3·70	3·65	3·66	3·64	3·28	3·67	3·57
Al_2O_3	13·41	14·39	14·63	14·80	14·54	11·68	11·83
FeO_{tot}	13·47	13·28	13·44	13·21	13·04	13·77	13·79
MnO	0·19	0·21	0·20	0·20	0·20	0·19	0·20
MgO	7·79	6·98	6·90	6·64	7·39	9·84	9·97
CaO	12·20	10·57	10·44	10·37	11·06	12·53	12·05
Na_2O	3·64	4·18	4·41	4·44	3·92	4·24	4·21
K_2O	1·58	1·94	1·98	2·01	1·69	1·73	1·78
P_2O_5	0·90	0·91	0·88	1·02	0·89	1·15	1·12
Rb	35·6	48·6	48·7	52	41·7	45·3	45·7
Sr	1223	1271	1214	1329	1025	1445	1431
Y	32·7	37·3	35·2	37·3	33·7	33·8	33·9
Zr	327	396	390	384	340	381	380
Nb	95	113	106	111	94	126	124
Cs	0·433	0·546	0·534	0·542	0·470	0·541	0·541
Ba	584	652	647	649	545	727	713
Ta	5·24	7·76	7·14	6·84	6·29	7·65	7·63
Tl	0·00	0·13	0·12	0·10	0·13	0·12	0·11
Pb	3·82	5·12	5·55	5·49	5·57	4·42	3·75
Th	10·52	8·54	8·07	8·12	8·05	9·29	9·37
U	2·53	2·32	2·21	2·57	2·12	2·55	2·80
Sc	29·3	21·5	21·3	22·9	25·1	24·1	23·5
V	367	302	309	318	318	337	324
Cr	299	258	199	228	283	438	455
Co	48·1	44·3	44·4	43·2	45·6	53·2	53
Ni	101	96	83	74	97	173	189
Cu	104	74	76	79	86	103	97
Zn	121	120	121	123	109	123	125
Ga	21	23	23	24	21	23	23
La	97	94	92	92	75	99	99
Ce	184	183	173	172	147	190	185
Pr	20·0	20·4	19·84	19·63	16·72	21·3	21·0
Nd	79	79	74	73	66	84	81
Sm	14·21	14·38	13·47	13·69	12·58	15·23	14·90
Eu	4·15	4·41	4·19	4·16	3·47	4·52	4·32
Gd	11·79	12·21	11·75	11·51	9·76	12·46	11·81
Tb	1·45	1·57	1·52	1·51	1·33	1·56	1·51
Dy	7·98	8·48	8·07	7·96	7·03	7·84	7·53
Ho	1·37	1·47	1·42	1·38	1·28	1·31	1·27
Er	3·30	3·69	3·41	3·58	3·43	3·25	3·18
Tm	0·411	0·483	0·484	0·480	0·478	0·394	0·405
Yb	2·51	2·72	2·49	2·58	2·72	1·99	2·04
Lu	0·345	0·346	0·333	0·343	0·358	0·254	0·273
Hf	7·88	8·55	8·05	7·85	6·85	7·84	8·08

(continued)

SiO_2 and Al_2O_3 (as well as the alkalis) increase. Marked inflections occur for many elements between 4 and 6 wt % MgO (Fig. 4). P_2O_5 also decreases with decreasing MgO after an initial moderate increase. We note that there is no distinction between the historical and prehistoric lavas in terms of their major element trends, as shown in Fig. 4.

On mantle-normalized, multi-incompatible element diagrams the basanites have relatively smooth, convex-upward patterns that typically peak at Nb–Ta followed by a steep negative slope from La to Lu (Fig. 5). Ubiquitous negative anomalies in both K and Pb characterize all of the lavas and they have high U/Pb (μ) ratios (Fig. 5). However, with increasing extent of differentiation the more evolved lavas also develop negative anomalies in Sr, P and Ti (Fig. 5). A selection of compatible and incompatible trace elements is plotted versus

MgO content in Fig. 6. Compatible trace elements such as Ni and Cr (not shown) exhibit a curvilinear decrease with decreasing MgO from 189 to 2 ppm and 613 to 2 ppm, respectively, whereas V and Sc (not shown) concentrations show a mild increase between 10 and 8 wt % MgO, after which they decrease rapidly. As Fig. 5 shows, incompatible elements such as Ba and Pb show a continuous curvilinear increase as MgO contents decrease. In marked contrast to this Nb, Sr, La and Yb all increase in concentration from 10 to 2 wt % MgO, but then either become invariant or decrease in concentration below 2 wt % MgO. As for the major element trends discussed above, no distinction is observed between the historical and prehistoric lavas in Fig. 6.

Sr and Nd isotope compositions show limited variation, with $^{87}Sr/^{86}Sr$ and $^{143}Nd/^{144}Nd$ ranging from 0·70308 to 0·70313 and 0·51289 to 0·51290, respectively

Table 2: Continued

Sample: Age:	TLP 32-1A prehistoric	TLP 32-1B prehistoric	TLP 36-1 prehistoric	TLP 37-1 prehistoric	TLP 38-1 prehistoric	TLP 44-1 prehistoric	TLP 64-1 prehistoric
SiO_2	43·53	43·59	43·01	43·80	43·87	42·94	44·05
TiO_2	3·72	3·79	3·40	3·55	3·51	3·74	3·59
Al_2O_3	13·67	14·35	13·78	15·41	15·23	13·34	15·15
FeO_{tot}	13·39	13·31	13·56	12·88	12·96	13·63	12·97
MnO	0·19	0·19	0·20	0·20	0·20	0·19	0·20
MgO	8·13	7·27	8·60	6·31	6·49	7·76	6·05
CaO	10·94	10·42	11·26	10·02	10·01	12·12	10·33
Na_2O	3·74	4·18	3·65	4·73	4·70	3·77	4·53
K_2O	1·77	1·92	1·52	2·10	2·07	1·62	2·07
P_2O_5	0·90	0·97	1·03	1·00	0·96	0·90	1·06
Rb	41·2	44·9	32·4	58	57	39·3	52
Sr	1291	1408	1227	1556	1501	1287	1345
Y	35·1	37·1	34·0	39·4	41·0	34·4	36·5
Zr	393	417	315	461	426	343	389
Nb	111	121	91	138	116	100	111
Cs	0·450	0·490	0·394	0·689	0·640	0·444	0·554
Ba	626	678	569	763	738	608	661
Ta	5·78	6·22	4·78	7·23	7·34	5·05	7·06
Tl	0·00	0·00	0·00	0·00	0·11	0·00	0·11
Pb	4·74	4·88	3·89	4·69	5·06	3·74	5·16
Th	10·80	11·59	8·71	11·83	10·34	10·04	8·01
U	2·98	3·19	1·88	3·20	2·92	2·48	2·70
Sc	27·2	24·2	25·0	20·4	20·0	30·2	20·9
V	349	353	323	327	297	376	295
Cr	241	198	310	131	136	282	151
Co	48·3	47·0	49·6	42·1	41·3	49·5	37·4
Ni	122	106	131	65	69	102	56
Cu	69	72	81	55	58	105	71
Zn	122	128	118	133	121	121	118
Ga	22	23	20	23	24	21	24
La	104	111	93	115	111	99	85
Ce	194	206	178	221	208	187	170
Pr	21·2	22·7	20·2	24·8	23·0	20·9	18·77
Nd	81	86	79	93	83	79	75
Sm	14·56	15·01	14·29	15·58	14·76	13·67	13·90
Eu	4·12	4·17	4·06	4·46	4·55	3·93	4·23
Gd	12·02	12·32	11·84	12·64	12·37	11·86	11·47
Tb	1·48	1·54	1·47	1·59	1·61	1·45	1·51
Dy	8·07	8·51	8·23	8·88	8·75	7·94	7·96
Ho	1·41	1·46	1·39	1·55	1·50	1·33	1·41
Er	3·40	3·51	3·46	3·74	3·88	3·25	3·70
Tm	0·437	0·435	0·447	0·508	0·521	0·417	0·496
Yb	2·47	2·60	2·59	2·77	3·02	2·36	2·73
Lu	0·351	0·352	0·360	0·400	0·390	0·338	0·368
Hf	8·78	9·06	7·17	9·63	8·35	7·68	8·01

(continued)

(Fig. 7a). The data are displaced towards the field of mid-ocean ridge basalts, with less radiogenic Sr and more radiogenic Nd than bulk Earth. Pb isotope compositions show slightly more variation, with $^{206}Pb/^{204}Pb$ ranging from 19·553 to 19·718, $^{207}Pb/^{204}Pb$ ranging from 15·597 to 15·612 and $^{208}Pb/^{204}Pb$ ranging from 39·296 to 39·528. These Pb isotope compositions effectively straddle the Northern Hemisphere Reference Line (NHRL; Hart, 1984) and extend toward HIMU, although they are not as radiogenic as basalts from St. Helena or Polynesia, which have $^{206}Pb/^{204}Pb > 20$ (Hauri & Hart, 1993). Overall, the new radiogenic isotope data fall within the fields previously reported from the Canaries (e.g. Elliott, 1991; Hoernle & Tilton, 1991; Hoernle *et al.*, 1991; Sigmarsson *et al.*, 1992; Thirlwall *et al.*, 1997; Thomas *et al.*, 1999; Praegel & Holm, 2006; Day *et al.*,

2010) but lie at the high $^{206}Pb/^{204}Pb$ end with a much more restricted range (Fig. 7b). There are no correlations between any of the radiogenic isotopes and indices of differentiation such as SiO_2 or MgO (not shown). Indeed, within the historical lavas, the most evolved phonolites have primitive Sr–Nd–Pb isotope ratios that are indistinguishable from those of the basanites and there is no distinction between historical and prehistoric samples (Fig. 7).

Th and U concentrations in the lavas range from 5·9 to 20 ppm and from 1·4 to 6·6 ppm, respectively, and show a curvilinear increase with decreasing MgO content (Fig. 8a and b). The $(^{234}U/^{238}U)$ ratios are generally within analytical error ($\pm6\permil$) of unity, suggesting that the samples have undergone minimal post-eruption alteration. We therefore assume all activity ratios to

Table 2: Continued

Sample: Age:	TLP 70-1 prehistoric	TLP 9-1 prehistoric	TLP 34-1 prehistoric	TLP 108-1 prehistoric	TLP 126-1 prehistoric	TLP 13-1 prehistoric	TLP 18-2 prehistoric
SiO_2	44·60	47·44	46·16	42·97	45·02	50·20	49·83
TiO_2	2·98	2·93	3·02	3·91	3·27	2·20	2·25
Al_2O_3	13·18	17·08	16·71	15·17	16·40	18·59	18·34
FeO_{tot}	12·43	10·42	11·38	13·65	12·12	8·40	8·61
MnO	0·19	0·20	0·20	0·21	0·21	0·19	0·20
MgO	9·47	3·95	4·62	5·56	4·96	2·53	2·75
CaO	11·19	8·53	8·83	10·69	9·56	6·84	7·10
Na_2O	3·67	5·92	5·56	4·21	5·16	7·11	7·02
K_2O	1·61	2·71	2·52	2·10	2·24	3·22	3·15
P_2O_5	0·69	0·82	0·99	1·54	1·06	0·73	0·75
Rb	40·2	80	75	47·6	59	109	105
Sr	979	1661	1533	1337	1374	1915	1862
Y	29·3	36·8	36·6	40·3	36·9	40·5	40·5
Zr	287	548	522	449	472	632	619
Nb	83	151	184	110	149	178	176
Cs	0·464	0·992	0·756	0·506	0·622	1·24	1·20
Ba	526	975	915	634	772	1133	1112
Ta	5·32	7·30	9·66	7·43	9·04	9·17	9·03
Tl	0·10	0·01	0·14	0·11	0·15	0·18	0·19
Pb	2·63	7·75	6·07	5·13	5·85	10·84	10·67
Th	7·11	16·78	12·15	7·34	9·56	18·53	18·47
U	2·06	4·72	4·19	2·04	3·03	5·84	5·77
Sc	27·3	15·1	15·5	17·2	16·7	7·2	7·7
V	272	255	257	273	250	177	176
Cr	613	12	33	8	28	3	4
Co	46·6	27	32	36	31	18	18
Ni	181	20	35	22	28	6	8
Cu	98	42	61	52	51	22	20
Zn	99	140	129	123	122	125	131
Ga	19	25	27	23	25	28	27
La	71	133	150	88	121	150	150
Ce	136	235	259	189	229	249	259
Pr	15·31	24·6	25·9	22·2	24·6	25·2	25·4
Nd	57	89	88	90	90	84	84
Sm	10·42	15·04	14·80	17·15	15·36	13·27	13·45
Eu	3·12	4·14	4·36	4·93	4·45	3·90	3·89
Gd	8·88	11·42	12·21	13·26	11·88	10·42	10·50
Tb	1·17	1·49	1·47	1·74	1·54	1·36	1·39
Dy	6·35	8·06	8·48	9·12	8·25	7·42	7·49
Ho	1·14	1·47	1·44	1·60	1·49	1·39	1·37
Er	2·88	3·74	3·48	4·28	3·98	3·63	3·69
Tm	0·398	0·491	0·475	0·561	0·546	0·519	0·521
Yb	2·30	3·06	2·70	3·04	3·01	2·92	2·99
Lu	0·309	0·435	0·375	0·393	0·418	0·407	0·406
Hf	6·11	11·26	9·79	9·68	9·92	9·78	10·13

(continued)

reflect magmatic processes. On the equiline diagram in Fig. 8c, the lavas have ^{230}Th excesses with ($^{230}Th/^{238}U$) ranging from 1·07 to 1·31. These excesses appear to be negatively correlated with SiO_2, at least for the historical samples (Fig. 9a). ^{226}Ra concentrations range from 786 to 3288 fg g^{-1} and ($^{226}Ra/^{230}Th$) from 1·01 to 1·63, and all of the prehistoric samples are clearly displaced to lower ($^{226}Ra/^{230}Th$) than the historical samples in Fig. 9b, suggesting that they are likely to be a few thousand years old. Furthermore, one of the prehistoric samples identified in Fig. 8c is within error of ^{226}Ra–^{230}Th secular equilibrium, such that its age is unconstrained and it could have undergone ^{230}Th decay since eruption. The samples that have measurable ^{226}Ra–^{230}Th disequilibria form a broad, positively inclined array to the left of the equiline whose slope would correspond to an age of ∼46 kyr. However, this is largely defined by three prehistoric samples with slightly elevated ($^{230}Th/^{232}Th$). Instead, the presence of ^{226}Ra–^{230}Th disequilibria in many of the samples (historical and prehistoric) and 1–2 kyr whole-rock–titanite isochrons for some of the phonolites (Johansen *et al.*, 2005) suggest that this array does not have age significance in any simple way (see further discussion below). An alkali gabbro cumulate (KLA 1-3-03) that was analysed for U-series isotopes only has a ($^{238}U/^{232}Th$) ratio of 0·53, a ($^{230}Th/^{238}U$) ratio of 2·15 and a ($^{226}Ra/^{230}Th$) ratio of 0·65. These ratios are similar to those of titanites analysed by Johansen *et al.* (2005) and so it is likely that the signal is dominated by the titanite present in this gabbro.

The new partition coefficient data are summarized in Table 6, with the full dataset reported in SD Electronic Appendix 3. The clinopyroxene and plagioclase

Table 2: Continued

Sample: Age:	TLP 46-1 prehistoric	TLP 69-1 prehistoric	TLP 116-1 prehistoric	TLP 19-2 prehistoric	TLP 10-1 prehistoric	TLP 27-1 prehistoric
SiO_2	47·17	47·31	47·75	51·12	57·50	56·04
TiO_2	2·99	2·83	2·84	2·02	0·71	0·86
Al_2O_3	17·04	17·05	17·34	18·79	20·58	20·73
FeO_{tot}	10·55	10·57	10·28	7·73	3·75	4·36
MnO	0·19	0·22	0·20	0·19	0·16	0·15
MgO	4·01	3·65	3·70	2·30	0·81	1·06
CaO	8·64	8·47	8·36	6·41	2·81	2·75
Na_2O	5·89	6·07	5·96	7·42	8·79	9·23
K_2O	2·70	2·70	2·74	3·37	4·69	4·60
P_2O_5	0·82	1·12	0·81	0·67	0·20	0·22
Rb	80	75	83	103	146	169
Sr	1605	1666	1593	1822	1020	2006
Y	37·4	38·4	36·5	33·3	18·8	23·7
Zr	510	549	515	618	808	1105
Nb	146	154	142	170	137	267
Cs	0·912	0·897	0·942	1·34	1·81	1·90
Ba	929	925	951	1143	1523	1641
Ta	8·13	7·84	8·66	7·71	4·02	9·98
Tl	0·15	0·00	0·14	0·03	0·11	0·20
Pb	8·14	4·16	8·57	10·39	14·88	26·2
Th	13·93	15·67	14·85	22·71	27·04	51·90
U	4·27	4·81	4·46	6·79	8·79	22·5
Sc	15·2	9·4	13·2	5·6	1·7	2·6
V	247	208	211	155	53	71
Cr	14	2	11	2	3	9
Co	28	22	23	15	4	6
Ni	23	6	17	4	2	6
Cu	49	21	41	15	4	8
Zn	117	145	113	133	119	129
Ga	26	26	25	26	29	35
La	132	128	125	152	135	180
Ce	230	233	226	252	183	250
Pr	23·2	25·3	23·1	25·3	14·69	21·3
Nd	82	94	83	86	44	64
Sm	13·61	15·91	14·10	13·03	5·62	8·49
Eu	4·08	4·56	4·09	3·68	1·64	2·30
Gd	11·43	12·24	11·06	9·90	4·32	6·12
Tb	1·45	1·61	1·46	1·33	0·61	0·85
Dy	7·92	8·85	7·86	7·51	3·78	5·11
Ho	1·36	1·56	1·41	1·36	0·76	0·94
Er	3·50	3·93	3·71	3·61	2·25	2·68
Tm	0·494	0·539	0·522	0·487	0·356	0·401
Yb	2·68	3·41	3·01	3·05	2·47	2·76
Lu	0·359	0·473	0·405	0·461	0·405	0·432
Hf	9·29	11·95	9·93	11·98	14·40	19·05

*Trace element data by XRF.
n.d., not determined.

partition coefficients are typically within the range reported in compilations such at that of Rollinson (1993). Partitioning of the rare earth elements (REE) into clinopyroxene increases significantly with increasing SiO_2, such that relative REE enrichment in the melt will decline with increased differentiation (see Brophy, 2008). Th is more compatible than U in the clinopyroxenes analysed (see Blundy & Wood, 2003). Nb and Ta are compatible in the analysed amphiboles, consistent with the findings of Ionov & Hofmann (1995) and Latourrette et al. (1995). Additionally, the REE are highly compatible in both apatite and titanite, and both favour Th over U. Nb and Ta are highly compatible in titanite, but not in apatite. These results are consistent with those reported in other recent studies of incompatible trace element partitioning into accessory phases (e.g. Wörner et al., 1983; Luhr et al., 1984; Prowatke & Klemme, 2006; Olin & Wolff, 2012) and should have utility well beyond the present study.

DISCUSSION

In the following sections we first briefly identify what constraints can be placed upon the conditions of generation of the parental magmas. Subsequently, we assess the effects of magmatic differentiation and appraise evidence for the timescales involved. These conclusions can be compared with published U-series isotope data and models for the other Canary Islands (Sigmarsson et al., 1992, 1998; Thomas et al., 1999; Lundstrom et al., 2003).

Table 3: XRF major (normalized to 100% anhydrous) and ICP-MS trace element data for plutonic rocks from La Palma*

Sample:	TLP 21-1A	TLP 30-2	TLP 52-9	TLP 52-10	TLP 52-12	TLP 52-14
SiO_2	49·51	35·65	46·79	48·62	64·18	64·88
TiO_2	0·62	5·41	3·74	3·00	0·48	0·61
Al_2O_3	12·98	12·52	18·26	18·03	18·73	19·25
FeO_{tot}	9·09	14·76	11·25	10·03	0·51	0·89
MnO	0·16	0·15	0·13	0·20	0·01	0·01
MgO	10·96	11·29	3·89	3·28	0·20	0·40
CaO	14·55	14·11	9·79	8·25	4·69	2·79
Na_2O	1·92	2·39	4·05	5·37	10·93	10·86
K_2O	0·18	1·07	1·57	2·27	0·09	0·07
P_2O_5	0·03	2·65	0·52	0·94	0·19	0·24
Rb	2·9	10·3	31·3	39·6	0·62	0·76
Sr	142	1239	1010	1138	155	327
Y	12·5	34·9	23·5	33·5	41·5	21·3
Zr	19	148	289	388	1980	899
Nb	3	52	67	110	414	174
Cs	0·034	0·083	0·318	0·758	0·03	0·01
Ba	28	528	429	620	11·5	30·9
Ta	0·18	2·93	3·93	7·42	34·2	16·6
Pb	1·64	1·35	2·34	3·69	1·28	2·25
Th	0·39	3·40	4·81	6·19	46·1	20·5
U	0·13	0·75	1·25	1·59	12·6	5·77
Sc	50	41	15	5	n.d.	n.d.
V	255	448	309	174	17	19·1
Cr	156	38	21	1	n.d.	n.d.
Co	42	57	31	16	n.d.	n.d.
Ni	83	75	39	1	n.d.	n.d.
Cu	13	42	180	2	n.d.	n.d.
Zn	56	99	100	123	4·15	8·47
Ga	12	18	24	22	29	24
La	4	67	47	68	41·5	47·4
Ce	8	145	94	144	79·7	86·4
Pr	1·10	18·38	11·06	17·25	8·39	9·04
Nd	5·42	82·52	45·60	70·83	28·4	29·1
Sm	1·75	16·55	8·74	12·77	5·63	4·56
Eu	0·77	4·99	2·94	3·65	1	1·32
Gd	2·19	14·25	7·51	10·84	5·35	3·6
Tb	0·39	1·75	1·02	1·47	1	0·55
Dy	2·70	9·03	5·75	8·08	6·59	3·36
Ho	0·59	1·51	1·04	1·42	1·42	0·73
Er	1·62	3·42	2·56	3·49	4·69	2·41
Tm	0·24	0·38	0·35	0·47	0·85	0·44
Yb	1·59	2·18	2·01	2·57	6·81	3·55
Lu	0·23	0·28	0·29	0·37	1·1	0·57
Hf	0·72	4·94	6·87	8·60	52	23·3

*Data in italics are from Johansen *et al.* (2005).
n.d., not determined.

Conditions of generation of the parental magmas

Unfortunately, none of the Cumbre Vieja lavas are close to primary liquids in equilibrium with mantle olivine; the most primitive basanite has Mg# = 63, 309 ppm Ni and 767 ppm Cr. Nevertheless, the magmas were clearly generated in the mantle and have steep REE patterns (Fig. 5) that suggest equilibration with residual garnet. Relatively high U/Pb and $^{206}Pb/^{204}Pb$ ratios suggest a HIMU-type source. However, the CaO versus MgO relationships in Fig. 4 are consistent with partial melting of peridotite followed by extended crystal fractionation and do not demand a role for recycled pyroxenite (see Sigmarsson *et al.*, 1998). P/Nd ratios of 50–60 in the basanites are also consistent with melting taking place in the garnet peridotite facies (O'Neill & Mallmann, 2007). Nevertheless, the radiogenic isotope data may require that the source had previously been metasomatized by melts from a recycled mafic component and the negative K anomalies in Fig. 5 could indicate that this component was formed in equilibrium with residual phlogopite (Elliott, 1991).

The ($^{230}Th/^{238}U$) and ($^{226}Ra/^{230}Th$) ratios are highest in the most mafic historical lavas, indicating that the disequilibria were created during mantle melting (see Sigmarsson *et al.*, 1992, 1998; Thomas *et al.*, 1999; Lundstrom *et al.*, 2003). The magnitude of the ^{230}Th excesses in mantle-derived melts is largely a function of the U and Th partition coefficients and the melting rate, which will be linked to the upwelling rate that controls the time available for ^{230}Th ingrowth during melting (e.g. Bourdon & Sims 2003). Garnet will retain U relative to Th in the mantle (e.g. Beattie, 1993) and the buoyancy flux of the Canary plume is low (Sleep, 1990), implying low upwelling rates (~3 cm a^{-1}). Thus, our data are

Table 4: Sr, Nd and Pb isotope data for La Palma rocks*

Sample	$^{87}Sr/^{86}Sr$	$^{143}Nd/^{144}Nd$	$^{206}Pb/^{204}Pb$	$^{207}Pb/^{204}Pb$	$^{208}Pb/^{204}Pb$
TLP 79-1	0·703118	0·512896	19·599	15·602	39·390
TLP 25-1	0·703099	0·512892	19·643	15·606	39·452
TLP 43-1	0·703108	0·512891	19·644	15·612	39·465
TLP 58-1	0·703107	0·512891	19·649	15·604	39·459
TLP 23-1	0·703088	0·512899	19·553	15·597	39·296
TLP 38-1	0·703117	0·512887	19·664	15·604	39·488
TLP 64-1	0·703102	0·512891	19·718	15·609	39·495
TLP 108-1	0·703099	0·512886	19·671	15·606	39·528
TLP 46-1	0·703129	0·512895	19·663	15·605	39·488
TLP 69-1	0·703082	0·512898	19·648	15·606	39·434
TLP 116-1	0·703127	0·512896	19·672	15·608	39·504
TLP 19-2	0·703125	0·512896	19·655	15·598	39·461
TLP 50-2	*0·703082*	*0·512898*	*19·651*	*15·601*	*39·438*
TLP 51-3	*0·703076*	*0·512897*	*19·659*	*15·602*	*39·450*
TLP 50-1	*0·703095*	*0·512892*	*19·661*	*15·604*	*39·472*
TLP 51-2	0·703099	0·512893	19·667	15·610	39·491

*Data in italics are from Johansen *et al.* (2005).

Table 5: U–Th–Ra isotope data for La Palma lavas

Sample	Th (ppm)	U (ppm)	Ra (fg g^{-1})	$(^{234}U/^{238}U)$	$(^{238}U/^{232}Th)$	$(^{230}Th/^{232}Th)$	$(^{230}Th/^{238}U)$	$(^{226}Ra/^{230}Th)_0$
TLP 79-1	6·49	1·90	1316	1·002	0·891	1·108	1·244	1·603
TLP 31-1	8·79	2·51	1464	1·008	0·868	1·085	1·250	1·426
KLA 1-5-08	6·00	1·73	986	1·027	0·872	1·105	1·267	1·452
KLA1-2-10	5·93	1·75	1070	1·007	0·884	1·124	1·285	1·401
KLA1-2-15	11·68	3·46	2100	1·016	0·898	1·113	1·239	1·443
KLA1-5-19	11·79	3·48	2132	1·005	0·896	1·099	1·227	1·505
KLA1-3-03*	8·20	1·43	687	1·002	0·531	1·139	2·151	0·647
TLP 111-1	8·53	2·36	2047	1·004	0·838	1·082	1·291	1·512
TLP 6-1	11·79	3·35	2349	1·008	0·864	1·087	1·259	n.d.
TLP 25-1	9·13	2·54	1592	1·008	0·845	1·079	1·276	1·530
TLP 43-1	8·74	2·37	1602	1·011	0·822	1·071	1·302	1·630
TLP 76-1	9·41	2·54	1760	1·013	0·820	1·077	1·313	1·614
TLP 58-1	8·44	2·41	1447	1·008	0·866	1·120	1·294	1·446
TLP 23-1	9·17	2·85	1156	1·002	0·945	1·120	1·184	n.d.
TLP 38-1	10·77	3·15	1606	0·999	0·888	1·149	1·294	1·168
TLP 64-1	8·86	2·92	1274	1·007	1·000	1·202	1·202	1·071
TLP 108-1	7·73	2·16	786	1·008	0·848	0·906	1·069	1·009
TLP 46-1	15·32	4·73	1249	1·009	0·936	1·130	1·207	1·225
TLP 69-1	13·62	4·61	1938	1·008	1·028	1·186	1·154	1·079
TLP 116-1	15·53	4·81	2319	1·004	0·939	1·154	1·229	1·149
TLP 19-2	20·44	6·64	3288	1·008	0·986	1·180	1·191	1·177

*Alkali gabbro nodule from the 1949 eruption.
n.d., not determined.

consistent with relatively slow melting rates in a melt column that penetrates the garnet stability zone. The magnitude of the ^{226}Ra excesses is typical of ocean island basalts in general and requires low porosity in the melting zone (e.g. Kokfelt *et al.*, 2003; Bourdon *et al.*, 2005; Koornneef *et al.*, 2012). More specifically, our U–Th–Ra data for the historical Cumbre Vieja lavas closely overlap those from other islands in the Canary Islands in Fig. 9b. For Lanzarote in the eastern part of the archipelago, Thomas *et al.* (1999) suggested 1–4% dynamic partial melting of lherzolite in the presence of 5% residual garnet, close to the garnet–spinel transition. It should be noted that these researchers also found no requirement for recycled mafic lithologies to explain their data. Given the overlap of published data from the other Canary Islands with those for the historical

Cumbre Vieja lavas in Fig. 9b, a similar model is applicable to La Palma. It may be that mantle melting conditions are relatively uniform across the Canary Islands, unlike the situation inferred for a number of other ocean island suites (e.g. Kokfelt *et al.*, 2003; Bourdon *et al.*, 2005; Koornneef *et al.*, 2012).

Fractional crystallization
The Cumbre Vieja lavas encompass a wide range in major and trace element compositions and there are a large proportion of intermediate rock compositions indicating extended differentiation prior to eruption. The coherency of the arrays in Figs 4 and 6 suggest that, to a first approximation, the magmas all evolved along a similar liquid line of descent from similar

Table 6: MELTS mineral assemblages and partition coefficients used in the trace element modelling*

Phase:	olivine	clinopyroxene 1	clinopyroxene 2	plagioclase	amphibole	spinel	titanite	apatite
MgO interval								
12–9 wt %	100	—	—	—	—	—	—	—
9–7 wt %	35	65	—	—	—	—	—	—
7–5 wt %	25	61	—	—	—	11	2	1
5–3 wt %	17	—	64		4	12	2	1
3–1 wt %	22	—	55	6	3	12	1	1
K_d								
V	0·1	1·53	5·60	n.d.	6·89	26	n.d.	1·48
Cr	—	1279	10·8	n.d.	15·9	—	n.d.	n.d.
Co	—	1·48	5·59	n.d.	8·97	—	n.d.	0·084
Ni	7·46	10·0	0·932	n.d.	2·06	29	n.d.	0·088
Cu	—	0·046	0·320	n.d.	0·135	—	n.d.	0·167
Zn	—	0·275	1·78	n.d.	2·83	—	n.d.	0·072
Rb	—	0·003	0·003	0·004	0·087	—	0·026	0·010
Sr	—	0·123	0·499	2·33	1·47	—	0·745	4·78
Y	—	0·741	2·57	0·003	2·48	—	63·9	19·0
Zr	—	0·464	1·44	<1E – 3	0·755	—	7·39	0·042
Nb	—	0·012	0·055	<1E – 3	1·28	—	29·8	0·010
Ba	—	0·001	0·001	0·344	0·951	—	0·001	0·038
Ra	—	5·7E – 05	4·0E – 05	0·065	0·076	—	0·001	0·038
La	—	0·111	0·518	0·068	0·588	—	20·7	15·9
Ce	—	0·200	0·912	0·043	0·977	—	38·2	18·5
Pr	—	0·321	1·43	0·030	1·48	—	56·0	22·6
Nd	—	0·460	2·08	0·026	2·14	—	78·5	27·4
Sm	—	0·713	3·02	0·015	3·06	—	99·4	30·4
Eu	—	0·766	3·14	0·192	3·19	—	94·0	28·4
Gd	—	0·877	3·44	0·010	3·44	—	108	29·5
Tb	—	0·877	3·30	0·006	3·24	—	97·6	25·5
Dy	—	0·884	3·24	0·004	3·10	—	86·9	22·4
Ho	—	0·855	3·01	0·003	2·82	—	75·3	19·9
Er	—	0·797	2·65	0·002	2·40	—	58·4	16·6
Tm	—	0·748	2·55	0·002	2·15	—	45·8	13·3
Yb	—	0·679	2·52	0·002	1·91	—	36·2	10·1
Lu	—	0·670	2·99	0·001	1·97	—	26·1	9·30
Hf	—	1·03	2·54	<1E – 3	1·27	—	12·6	0·018
Ta	—	0·054	0·213	<1E – 3	1·18	—	95·6	0·004
Pb	—	n.d.	n.d.	n.d.	0·224	—	0·048	0·500
Th	—	0·015	0·027	<1E – 3	0·028	—	7·58	2·08
U	—	0·007	0·015	<1E – 3	0·020	—	2·87	1·27

*Partition coefficients are as measured in the La Palma rocks (see Supplementary Data Electronic Appendix 3) with the exception of those for V and Ni in olivine and spinel, which were taken from Rollinson (1993). Ra partition coefficients were either assumed to be the same as for Ba (apatite and titanite) or in the case of the other phases calculated from the Ba partition coefficients following the methods of Blundy & Wood (2003).
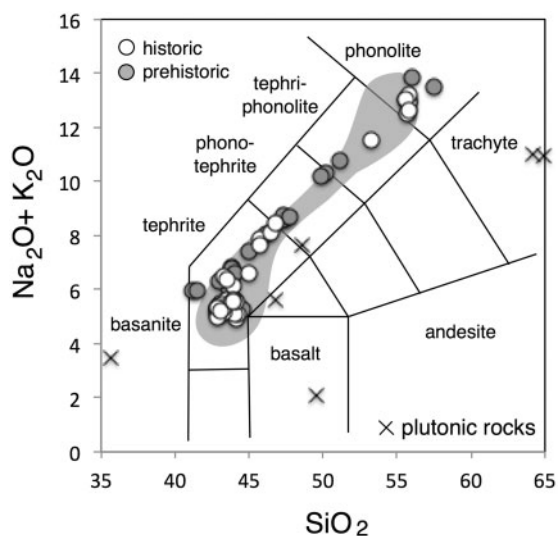
Fig. 3. Total alkalis–silica diagram for Cumbre Vieja volcanic rocks and possible basement contaminants (crosses). Rock classification after Le Bas *et al.* (1986). Shaded field is for data from Hernandez-Pachero & Valls (1982), Hernandez-Pachero & De La Nuez (1983), Elliott (1991) and Klügel *et al.* (2000).

parental magmas, which implies differentiation under similar pressure–temperature conditions. There is little variation in the radiogenic isotope data (Fig. 7) and no correlation between radiogenic isotope compositions and indices of differentiation such as SiO_2 or MgO, suggesting that a simple model of closed-system fractional crystallization may be applicable. Additionally, the curvilinear or inflected arrays for many elements are consistent with changes in the mineralogy of the fractionating assemblage and preclude models involving two end-member mixing for the whole suite, even though mixing of magmas has been inferred to be an important process in the petrogenesis of Cumbre Vieja lavas (Klügel *et al.*, 2000) and especially for the more differentiated types (see below).

Accordingly, we have used MELTS (Ghiorso & Sack, 1995; Gualda & Ghiorso, 2014) to calculate a liquid line of decent for the composition of the most primitive basanite (KLA 1-5-13) reported by Klügel *et al.* (2000). The
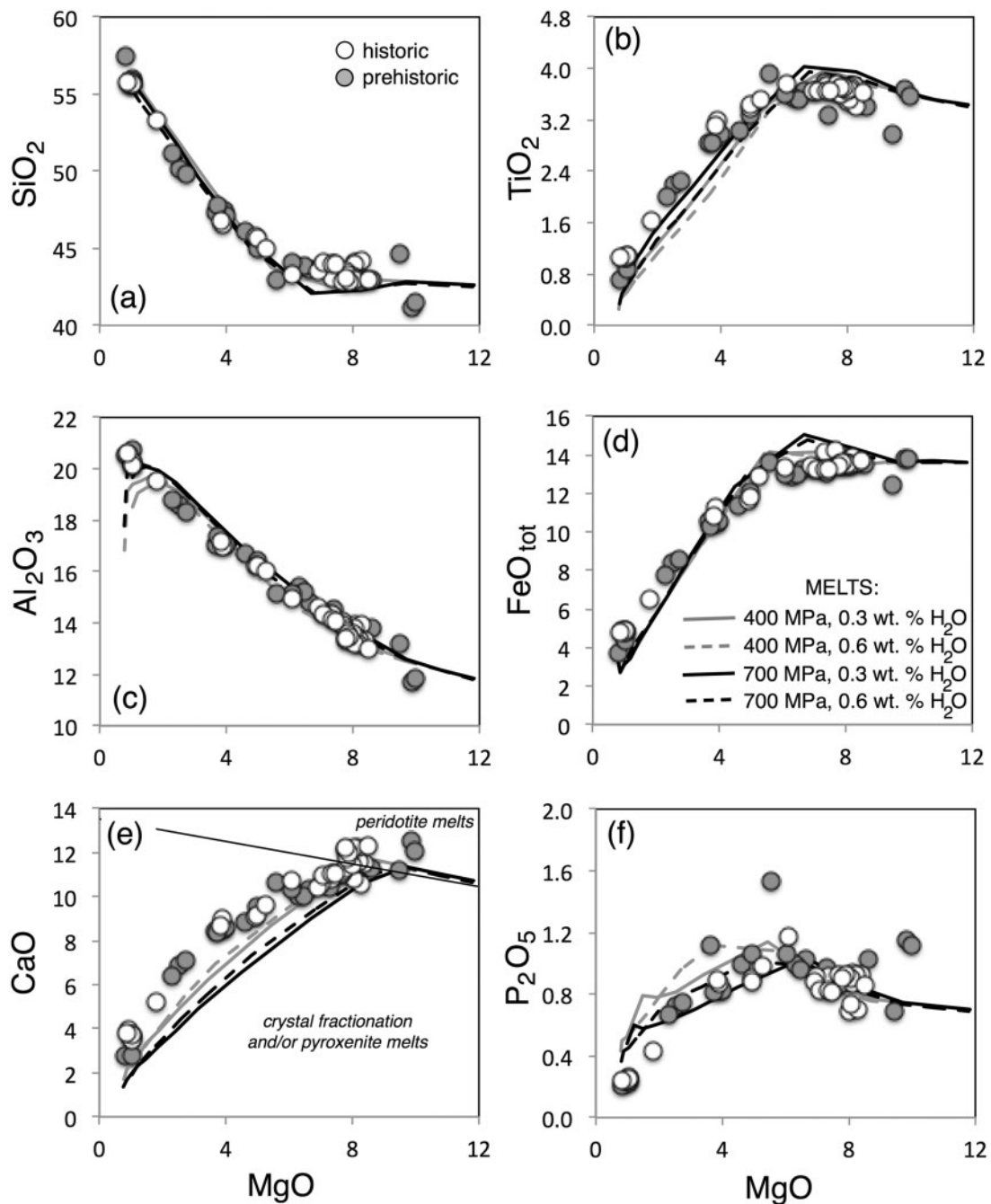
Fig. 4. Major element variation diagrams showing the coherency of the Cumbre Vieja volcanic rocks with liquid lines of descent calculated using MELTS (Ghiorso & Sack, 1995) superimposed. Conditions of the MELTS simulation were 400–700 MPa pressure and 0·3–0·6 wt % H_2O at the QFM buffer. The fine straight line on the CaO–MgO plot is the peridotite–pyroxenite melt dividing line of Herzberg & Asimow (2008).

chosen conditions for the simulation were 400–700 MPa pressure, based on evidence from Klügel et al. (2000, 2005), 0·3–0·6 wt % H_2O, based on the ubiquitous presence of kaersutitic amphibole, and redox conditions at the QFM buffer. Over the temperature interval ~1320–950°C, SiO_2 in the liquid increases continuously and the fractionating assemblage sequentially involves olivine, olivine + clinopyroxene, olivine + clinopyroxene + spinel + apatite and olivine + clinopyroxene + plagioclase + spinel + apatite in varying proportions.

Amphibole and biotite were present only in the runs performed with 0·6 wt % H_2O and titanite was not present at all. We emphasize that these model assemblages show some differences from the actual petrography, highlighting issues with the ability of MELTS to predict saturation of some phases.

The results of the MELTS modelling are superimposed on the major element variation diagrams in Fig. 4 and, with the above caveats in mind, the MELTS model clearly provides a good first approximation of
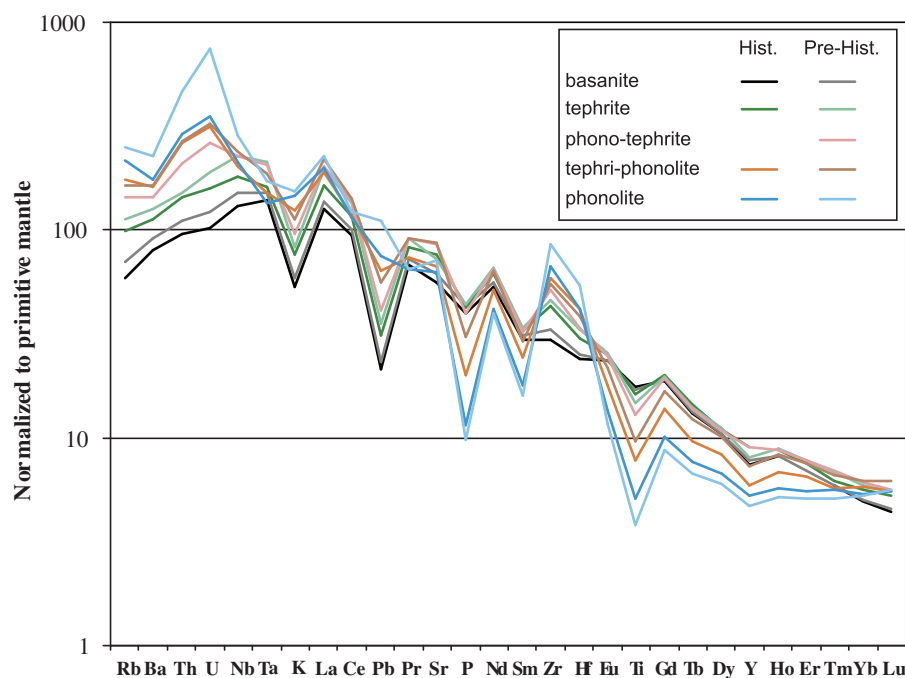
Fig. 5. Primitive mantle-normalized multi-element diagram (Hofmann, 1988) for averages of the compositional groups, subdivided into prehistoric and historical eruptions.

the major element data across the compositional range from basanite to phonotephrite. We note that Al_2O_3 begins to decrease below MgO = 2 wt % in the 0·6 wt % H_2O models and cannot replicate the phonolite compositions as well as the runs performed with 0·3 wt % H_2O. Similarly, the lower pressure runs arguably provide better simulations of the data for CaO (although perhaps not P_2O_5). This must be a compositional effect, as higher total pressures and water contents will normally delay saturation of plagioclase and favour precipitation of amphibole. Nevertheless, the best MELTS simulation of the evolution from basanite to phonolite for the Cumbre Vieja lavas is at 400 MPa and 0·3 wt % H_2O, including replication of the variations in N_2O and K_2O (not shown). This is consistent with the observation that clinopyroxene is cotectic with olivine rather than plagioclase in the basanites and this occurs only at pressures ≥400 MPa (e.g. Fisk *et al.*, 1988). For the preferred model, the liquid fraction (*F*) decreases by 85% over the temperature interval 1320–990°C. These results are entirely consistent with the suggestions of Klügel *et al.* (2005) that the magmas largely differentiated in the upper mantle followed by stalling at shallower levels for short durations, where the evolution of the intermediate magmas to produce phonolites occurs.

To further appraise the closed-system fractionation model, we undertook Rayleigh fractionation modeling of the trace element data using the composition of the most primitive basanite, the mineral modes derived from the preferred MELTS model in 2 wt % MgO increments and our measured partition coefficients as detailed in Table 6. The latter were supplemented by data

for olivine and spinel from Rollinson (1993) and we used the methods of Blundy & Wood (2003) to calculate the Ra partition coefficients (see Table 6). We included some amphibole and titanite in the final stages of crystallization to remain consistent with the petrography and also performed a second set of calculations in which we used the mineral and melt proportions Johansen *et al.* (2005) derived from least-squares models for the Cumbre Vieja lavas. As illustrated in Figs 6 and 8, the results from the two models are very similar for most elements and provide a good simulation of the data over the compositional range from basanite to phonotephrite–tephriphonolite (12–5 wt % MgO). However, the models fail in a number of respects at lower MgO and higher SiO_2 (i.e. for the evolution from tephriphonolite to phonolite). Most notably, the observed increases in Ba, Pb, Th and U concentrations and the associated decrease in Sr concentration during the late stages of differentiation are not reproduced. Similarly, the inflected trend for Yb is not replicated at all.

Incompatible element behavior during the evolution of the phonolitic magmas

Carbonatites are found on some of the Canary Islands (Hoernle *et al.* 2002) and one means to produce phonolite magma involves separation of an immiscible carbonatite liquid, which can lead to significant chemical fractionation (e.g. Freestone & Hamilton, 1980; Kogarko, 1997). However, available partitioning data (Jones *et al.*, 1995) indicate that this will produce [226]Ra deficits in the phonolite magma that are not observed in our samples. Moreover, the phonolites form a
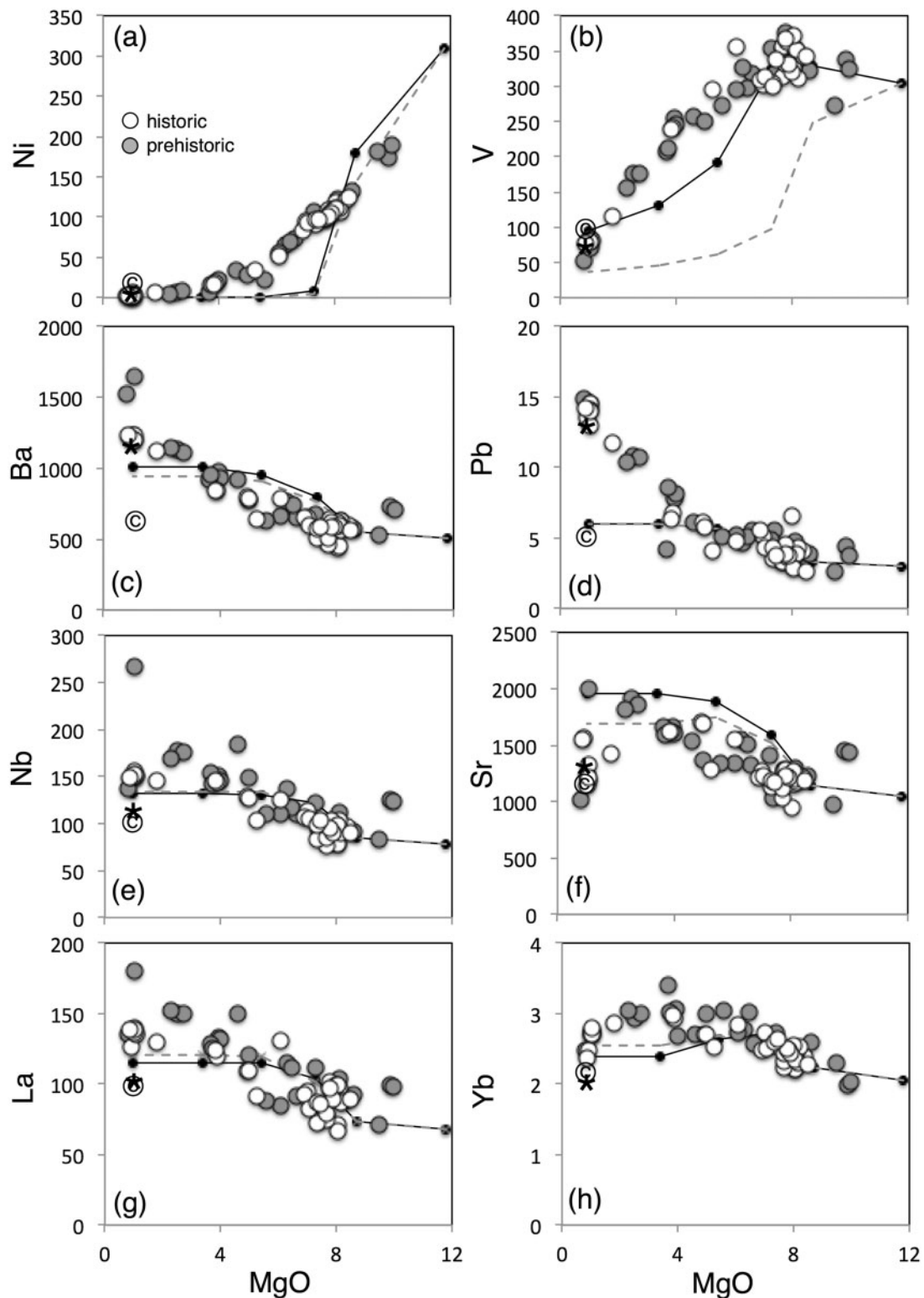
Fig. 6. Plots of trace elements, chosen for their varying compatibility, vs MgO. Model curves are for Rayleigh fractionation of the most primitive basanite using the partition coefficients listed in Table 6. Continuous curves used the mineral modes and melt proportions from the preferred MELTS model reported in Table 6. The dashed curves used the same partition coefficients but mineral modes and melt proportions based on least-squares modelling by Johansen *et al.* (2005). The composition resulting from addition of 17% partial melt of a phonotephrite to the basanite glass in Table 7 is indicated by the star, whereas addition of 17% partial melt of a cumulate from the phonotephrite to the basanite glass is indicated by ©. (See text for discussion.)
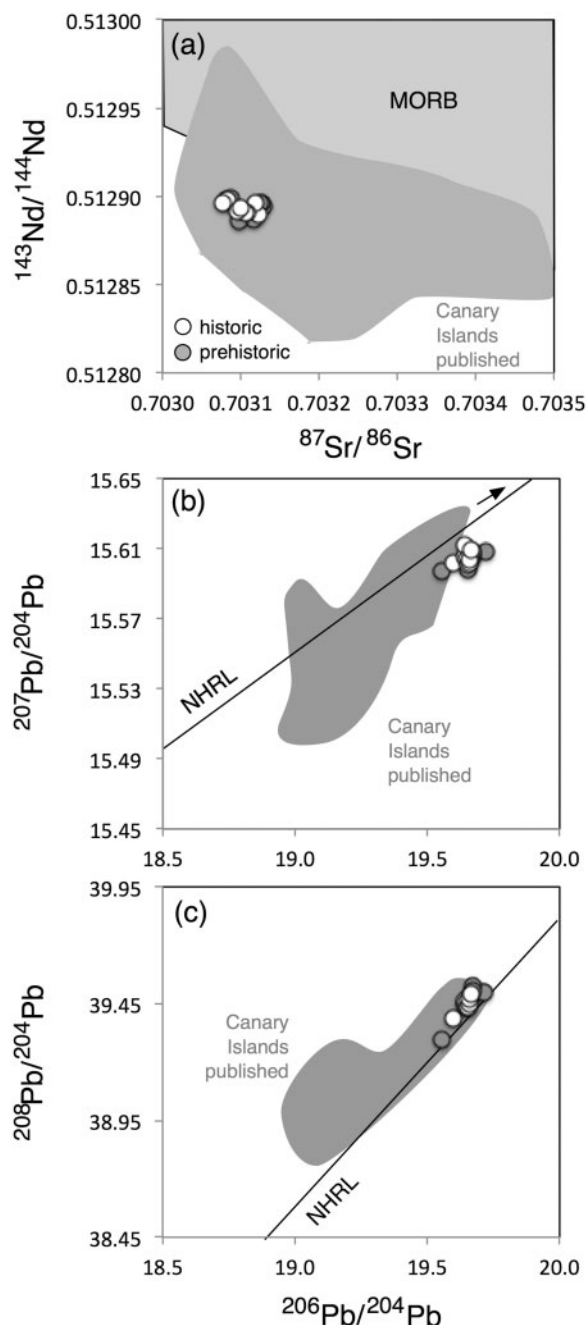
Fig. 7. Variation of (a) ^{143}Nd/^{144}Nd vs ^{87}Sr/^{86}Sr, (b) ^{207}Pb/^{204}Pb vs ^{206}Pb/^{204}Pb and (c) ^{208}Pb/^{204}Pb vs ^{206}Pb/^{204}Pb for the Cumbre Vieja volcanic rocks. Grey fields are literate data from the Canary Islands (Hoernle et al., 1991; Sigmarsson et al., 1992; Thirlwall et al., 1997; Thomas et al., 1999; Praegel & Holm, 2006). MORB field on (a) is from Yu et al. (1997) and the arrow on (b) points to HIMU. Northern Hemisphere Reference Line (NHRL) from Hart (1984).

compositional continuum with the other lavas (Figs 4 and 6) that is more consistent with an origin through differentiation and/or late stage mixing.

Over several decades, a number of canonical incompatible trace element ratios have been identified that appear to be largely invariant within oceanic basalts. One of the striking observations from the Cumbre

Vieja data is that whereas some of these ratios, such as La/Nb, K/Rb, Ba/Th and Ba/Nb, are relatively invariant across the differentiation sequence, others such as Nb/U, Ce/Pb, Nd/Pb, Nb/Ta, Zr/Hf and La/Ce show marked variation below ∼6 wt % MgO. As an example, the contrasting behavior of La/Nb and Ce/Pb is illustrated in Fig. 10a and b. Neither olivine, pyroxenes or plagioclase can significantly affect these ratios, but it is possible that the departure of many ratios from their canonical values reflects amphibole and late-stage accessory phase fractionation, as these are common phases in both lavas and cumulate nodules on La Palma. We choose to illustrate this largely based on discussion of the controls on Nb/U (Fig. 10c–f) because a feature that Lundstrom et al. (2003) noted in their compilation study of lavas from the Canary Islands is that Nb/U ratios vary well beyond the canonical value of 47 ± 10 that is characteristic of both mid-ocean ridge and ocean island basalts (Hofmann et al., 1986).

As shown in Fig. 10c, below about 5 wt % MgO, Nb/U ratios show a decrease from ∼50 to ∼10 in the phonolites. Amphibole and titanite are some of the few minerals that have high Nb/U (see Table 6) and can, therefore, produce decreases in Nb/U ratios via fractional crystallization. Recently, Davidson et al. (2013) have highlighted the utility of Dy/Dy*, as a measure of the curvature of REE patterns, to identify the role of amphibole fractionation; however, in alkaline magmas this ratio can also be decreased by fractionation of titanite (Wörner et al., 1983; Olin & Wolff, 2012). As shown in Fig. 10d, the decreases in Nb/U are strongly correlated with decreasing Dy/Dy* in the Cumbre Vieja lavas, providing good evidence for fractional crystallization of amphibole. However, although there is a positive correlation between Nb/U and Dy/Dy*, both of the numerical models illustrated in Fig. 10d are incapable of replicating the full extent of the Cumbre Vieja array. The same is true for the decrease in Ce/Pb below 5 wt % MgO, even though both apatite and titanite were included in the models (Fig. 10b, Table 6).

Mixing with partial melts of plutonic rocks

Interaction with crustal rocks provides another means to explain the departure of the evolved lavas from the modelled liquid line of descent. However, the lack of variation in the radiogenic isotopes requires that this involve earlier equivalents of the lavas rather than any exotic component such as continental crust or sediment, consistent with the tectonic setting. The analysed plutonic rocks span a significant range in Nb/U ratios and these are lowest at low MgO, supporting a potential role for such materials in the generation of the evolved Cumbre Vieja lavas (Fig. 10c). The leverage of residual clinopyroxene and accessory phases can be significant during relatively small degrees of partial melting, and in the following discussion we explore two scenarios for generating the trace element trends at <5 wt % MgO: (1) partial melting of the
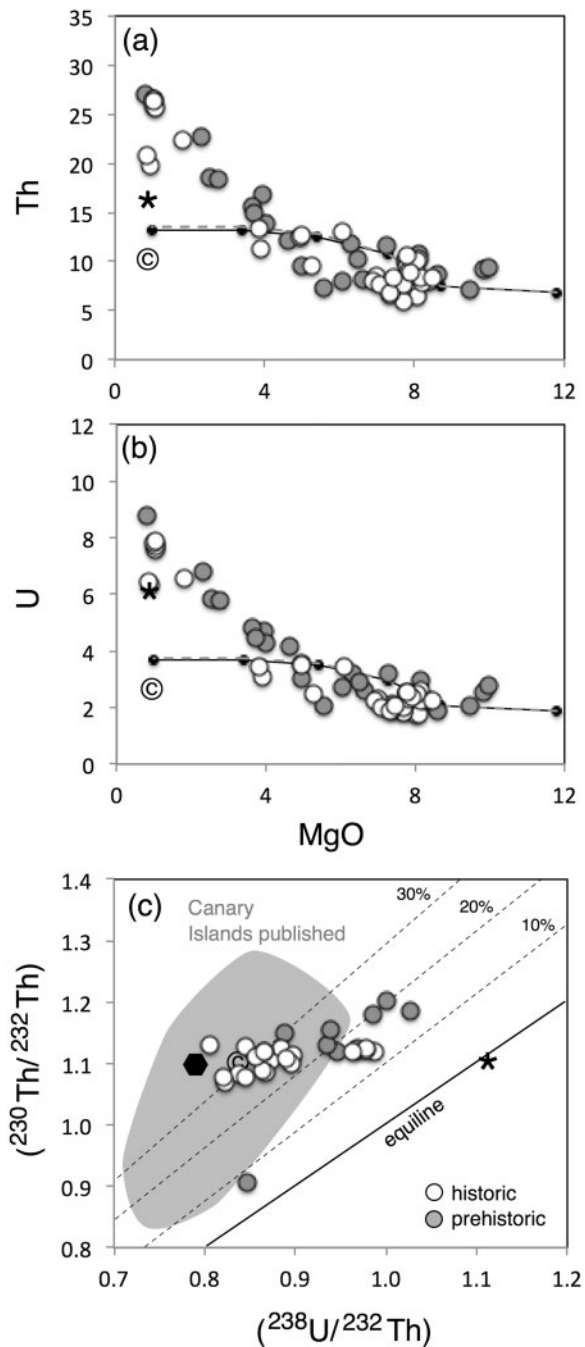
Fig. 8. (a, b) Variation of Th and U vs MgO along with curves for the same models as shown in Fig. 6. It should be noted that sample TLP 27-1 with 52 ppm Th and 26 ppm U plots outside the scale of these diagrams. (c) U–Th equiline diagram for historical [including published data from Johansen *et al.* (2005)] and prehistoric eruptions of Cumbre Vieja, La Palma (dashed lines indicate 10, 20 and 30% ^{230}Th excess). It should be noted that one prehistoric sample in (c) has ^{226}Ra–^{230}Th within error of secular equilibrium and so it is likely that its low (^{230}Th/^{232}Th) ratio reflects decay since eruption (see also Fig. 10b). Grey field on (c) is literate data from the Canary Islands from Lundstrom *et al.* (2003). The black hexagon represents a dynamic peridotite melt calculated using the formulation of Williams & Gill (1989) and the following parameters: extent of melting 4%, melt column length 150 km, upwelling rate 3 cm a^{-1}, solid density 3300 kg m^{-3}, melt density 2800 kg m^{-3}, source contains 3·4 ppb U, 13·7 ppb Th, 57% olivine, 23% orthopyroxene, 15% clinopyroxene and 5% garnet such that
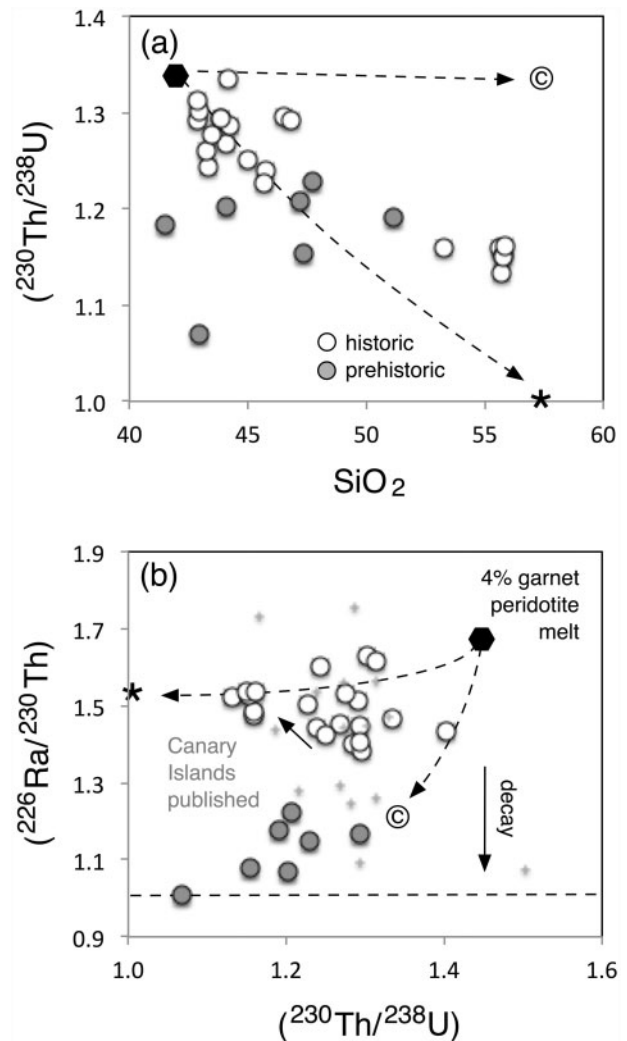
Fig. 9. (a) Variation of (^{230}Th/^{238}U) vs SiO$_2$ (wt %). (b) Plot of (^{226}Ra/^{230}Th) vs (^{230}Th/^{238}U). The inclined arrow in (b) shows the magnitude and direction of the shift owing to fractional crystallization involving accessory phases based on the models in Fig. 6; decay during ageing is indicated by the downward vertical arrow. Grey field on (b) is literate data from the Canary Island from Lundstrom *et al.* (2003) and the horizontal dashed line indicates secular equilibrium. The black hexagon in (b) is the same dynamic melt as shown in Fig. 8c assuming $D_{Ra} = 8 \times 10^{-7}$ based on Blundy & Wood (2003). The composition resulting from addition of 17% partial melt of a phono-tephrite to the basanite glass in Table 7 is indicated by the star, whereas addition of 17% partial melt of a cumulate from the phonotephrite to the basanite glass is indicated by ©. Mixing vectors are indicated by the arrowed dashed curves.
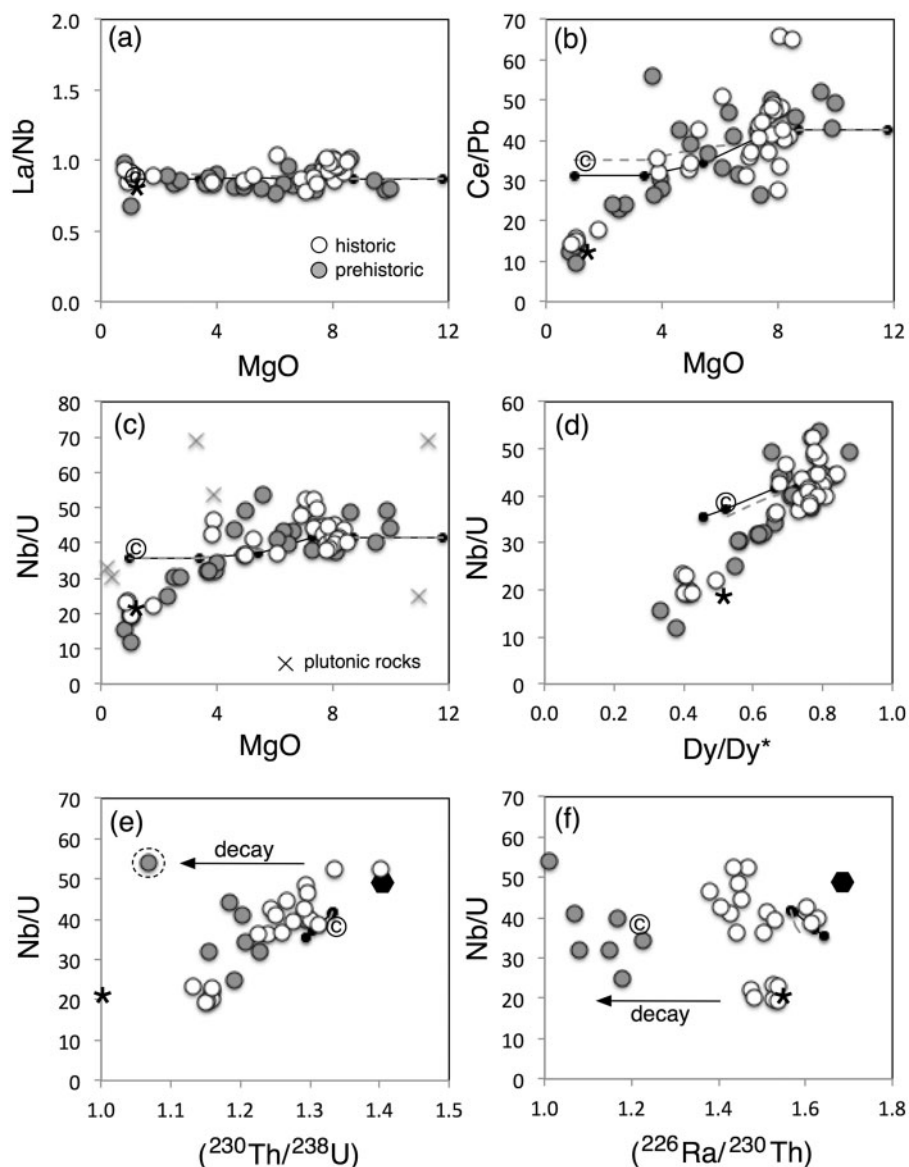
$D_U = 3·96 \times 10^{-3}$ and $D_{Th} = 1·76 \times 10^{-3}$ based on the 3 GPa partition coefficients of Blundy & Wood (2003). The composition resulting from addition of 17% partial melt of a phonotephrite to the basanite glass in Table 7 is indicated by the star, whereas addition of 17% partial melt of a cumulate from the phonotephrite to the basanite glass is indicated by ©.

Fig. 10. Variation of (a) La/Nb vs MgO, (b) Ce/Pb vs MgO, (c) Nb/U vs MgO, (d) Dy/Dy* vs Nb/U used as an indicator of amphibole fractionation (Davidson *et al.*, 2013), (e) (^{230}Th/^{238}U) and (f) (^{226}Ra/^{230}Th) vs Nb/U. It should be noted that the prehistoric lavas have undergone significant decay of ^{226}Ra in (f), and one of these samples in (e), which has (^{226}Ra/^{230}Th) = 1, has probably experienced ^{230}Th decay. The curves are derived from the same models as depicted in Fig. 6 and discussed in the text. For (e) and (f) the parental magma with (^{230}Th/^{232}Th) = 1·1 and (^{226}Ra/^{230}Th) = 1·68 comes from the model described in the caption to Figs 8 and 9. The composition resulting from addition of 17% partial melt of a phonotephrite to the basanite glass in Table 7 is indicated by the star, whereas addition of 17% partial melt of a cumulate from the phonotephrite to the basanite glass is indicated by ©.

intrusive equivalents of the more primitive phonotephrites (i.e. syenite); (2) partial melting of cumulates formed during the generation of the more primitive phonotephrites (note that this latter component needs to be a melt of a solid cumulate rather than melt present in a crustal mush, as the latter would simply lie on the modeled liquid lines of descent).

Table 7 lists the composition of a phonotephrite glass (analysed in basanite Pos270 164-7) provided in SD Electronic Appendix 3. As detailed in Table 7, we have calculated the composition of a 10% partial melt of this composition and also a 10% melt of an inferred cumulate from this glass composition, using the mineral modes

listed. On the basis of solubility data from Hellman & Green (1979) and Watson (1979) it was assumed that titanite, but not apatite, would be a residual phase, along with olivine, pyroxene, plagioclase and amphibole. We did not include spinel in the calculations, but the low partition coefficients for the elements of interest mean that this will not alter the outcomes of the modeling. As can be seen in Table 7, the Ce/Pb, Nb/U and Dy/Dy* ratios of the partial melt of the model syenite are significantly lower than those of the glass, whereas La/Nb remains relatively unchanged. In contrast, the Ce/Pb and Nb/U ratios of the model cumulate and a partial re-melt thereof are significantly higher than those of the glass. As shown

Table 7: Crustal melting models (see text for explanation)*

ppm	Pos270 164-7 basanite glass	10% melt of rock	56% cumulate	10% melt of cumulate
Ni	5	3	6	4
V	102	28	175	48
Rb	52	471	0·8	7
Ba	686	3442	106	532
Ra*	1272	11207	296	2611
Th	10·4	41·1	2·4	9·6
U	3·01	18·67	0·29	1·81
Nb	110	151	86	118
La	96	119	82	101
Ce	178	131	217	159
Pb	5·8	52·6	0·10	0·94
Sr	1241	1504	1072	1300
Nd	65	23	106	38
Sm	10·8	2·9	18·6	4·9
Zr	307	279	328	298
Hf	5·57	3·02	7·92	4·29
Gd	7·44	1·78	12·97	3·10
Tb	1·03	0·26	1·78	0·46
Dy	5·61	1·53	9·63	2·62
Y	25·4	8·94	41·64	14·65
Yb	2·31	1·01	3·57	1·56
Lu	0·33	0·14	0·52	0·22
La/Nb	0·87	0·79	0·95	0·86
Ce/Pb	30	2·5	2089	170
Nb/U	37	8	293	65
Dy/Dy*	0·57	0·26	0·76	0·35
$(^{238}U/^{232}Th)$	0·88	1·38	0·37	0·57
$(^{230}Th/^{232}Th)$	1·10	1·10	1·10	1·10
$(^{226}Ra/^{230}Th)*$	1·00	2·23	1·00	2·23

*All models assumed a residual assemblage composed of 12% olivine, 64% clinopyroxene, 17% plagioclase, 5% amphibole and 2% titanite, and used the partition coefficients from Table 6. Ra concentrations were calculated assuming secular equilibrium with $(^{230}Th/^{232}Th) = 1·1$.

in Figs 6 and 8–10, mixing of ∼17% of the partial melt of the model syenite into an newly intruding phonotephrite provides a reasonable first-order approximation of the departure of the more evolved lavas from the modeled liquid line of descent. Detailed appraisal of the diagrams indicates that the relative contributions of the two components (and/or proportions of residual phases) must be variable from one lava to another, but that is hardly surprising. More importantly, mixing with the model cumulate re-melt would lead to lower Ba, Pb, Th and U concentrations and higher Ce/Pb and Nb/U than observed and so cannot explain the observed trends. In summary, we conclude that closed-system fractional crystallization from 12–5 wt % MgO followed by differentiation combined with mixing with partial melts of earlier formed syenites in the presence of residual amphibole and titanite can explain the general trends observed in the Cumbre Vieja lavas.

We now return to the U-series data to obtain constraints on the timescales involved.

U-series isotope behaviour and differentiation timescales

A striking observation in Fig. 10e is that the decreases in Nb/U are correlated with decreasing $(^{230}Th/^{238}U)$. One possible explanation is that differentiation was accompanied by assimilation of crustal materials that had low Nb/U and were also sufficiently old to be in $^{230}Th-^{238}U$ secular equilibrium. However, the lavas form a broadly horizontal array on the equiline diagram (Fig. 8c), requiring that both end-members in any mixing scenario have the same $(^{230}Th/^{232}Th)$ ratios, as decay would result in significantly lower $(^{230}Th/^{232}Th)$. This requires that the syenites implicated in the model described above would have to be less than ∼10 kyr old such that their $(^{230}Th/^{232}Th)$ ratios remained essentially unchanged from those of newly intruding magmas. Making this assumption, Fig. 8c shows the calculated U-series composition of the melts from Table 7. Once again, it is clear that the cumulate re-melt cannot replicate the range of the data when mixed with the inferred primary melt whereas mixing with the syenite melt can. The same conclusions hold for the relationships in Figs 9a and 10e. It should be noted that because Th is more compatible than U in the fractionation assemblage (Table 6) crystal fractionation will also drive compositions to higher $(^{238}U/^{232}Th)$ but, again, this must occur on a timescale less than 10 kyr to maintain the broadly horizontal array in Fig. 8c. This is strongly supported by the data for the alkali gabbro cumulate, which has a very low $(^{238}U/^{232}Th)$ ratio of 0·53 yet a $(^{230}Th/^{232}Th)$ ratio of 1·1, similar to the majority of the lavas (Table 5).

A further and equally important feature of the data is that although the fractionation followed by mixing model can adequately explain the correlated decreases in Nb/U (and Ce/Pb and Dy/Dy*), there is little or no associated change in $(^{226}Ra/^{230}Th)$ within the historical lavas across the whole range in Nb/U ratios (Fig. 10f). This highlights the importance of residual titanite, in which Th is significantly more compatible than either Ra or U (Table 6). The result is that the syenite melts are displaced to much higher $(^{238}U/^{232}Th)$ and are also predicted to have considerable ^{226}Ra excesses (see Table 7). Thus, addition of these melts will pull the evolved lavas towards the equiline in Fig. 8c, yet have a much more muted affect on their $(^{226}Ra/^{230}Th)$ ratios and, at most, cause a 10–20% decrease in the ^{226}Ra excesses (see Figs 9b and 10f). Small but variable amounts of decay or accessory phase fractionation combined with variations in the disequilibria in the incoming lavas can readily explain the remaining variation in the observed U-series disequilibria. The important corollary is that the combined timescale for crystal fractionation and mixing cannot have been be much longer than the half-life of ^{226}Ra (1600 years) and this is entirely consistent with the 1–2 kyr internal isochrons reported by Johansen *et al.* (2005).

The timescales we infer for small-volume phonolite generation on La Palma are in good agreement with the findings of Lundstrom *et al.* (2003), Johansen *et al.* (2005) and Reagan *et al.* (2008). The timescales are also broadly consistent with the observations of Blake & Rogers (2005), with the implication that the power output of many small to moderate-sized magmatic systems

is consistent with their location in the shallow to mid-crust ($\sim$13 km depth in the case of the formation of the evolved La Palma lavas), where cooling and crystallization are likely to be relatively rapid (Dosseto *et al.*, 2008; Turner *et al.*, 2010). Phonolite evolution in volcanic systems such as Laacher See would appear to involve longer timescales of tens of thousand years that are consistent with their large ($\sim$6·3 km^3) volume (Bourdon *et al.*, 1994; Schmitt *et al.*, 2010). Overall, the combined observations fit into a model of repeated magma injection and rapid extraction of different melt batches beneath the Cumbre Vieja rift system (Klügel *et al.*, 2000, 2005).

CONCLUSIONS

A study of the geochemistry of historical and prehistoric Cumbre Vieja lavas that span a wide range of compositions from basanite to phonolite indicates an evolutionary process initially involving closed-system fractional crystallization of magmas produced by small-degree partial melting of garnet lherzolite followed by mixing with melts of young syenites (Klügel *et al.*, 2000). More complex models invoking interaction with amphibole-bearing lithospheric mantle, assimilation of old syenitic crust or separation of an immiscible carbonatite liquid from the phonolite magmas do not seem required by the data and radiogenic isotope ratios show little variation. Incompatible trace element data indicate an important role for titanite during the later stages of differentiation, which produced marked changes in trace element ratios, such as Ce/Pb and Nb/U, that are normally considered invariant in oceanic basalts (e.g. Hofmann *et al.*, 1986). Thus, paradoxically, MgO, Nb/U and (^{230}Th/^{238}U) all decrease together whereas (^{226}Ra/^{230}Th) remains unaffected. Nevertheless, the U-series isotope data indicate that differentiation occurred over a few hundred years to 2000 years and this is consistent with evidence for rapid magma ascent (Klügel *et al.*, 2000) and the results of other recent U-series isotope studies of basanite to phonolite evolution in ocean islands (e.g. Johansen *et al.*, 2005; Reagan *et al.*, 2008). The implication is that such lavas evolve from relatively small magma batches that differentiate in the mantle and are then repeatedly emplaced into the mid- to shallow crust of the Cumbre Vieja rift system, where cooling and crystallization are likely to be relatively rapid. The resultant magmas are then rapidly extracted to be erupted at the surface (e.g. Klügel *et al.*, 2000).

ACKNOWLEDGEMENTS

FUNDING

SUPPLEMENTARY DATA

Supplementary data for this paper are available at *Journal of Petrology* online.

REFERENCES

Ancochea, A., Hernán, F., Cendrero, A., Cantagrel, J. M., Fúster, J. M., Ibarrola, E. & Coello, J. (1994). Constructive and destructive episodes in the building of a young oceanic island, La Palma, Canary Islands, and genesis of the Caldera de Taburiente. *Journal of Volcanology and Geothermal Research* **60**, 243–262.

Annen, C., Blundy, J. D. & Sparks, R. S. J. (2006). The genesis of intermediate and silicic magmas in deep crustal hot zones. *Journal of Petrology* **47**, 505–539.

Beattie, P. (1993). Uranium–thorium disequilibria and partitioning on melting of garnet peridotite. *Nature* **363**, 63–65.

Blake, S. & Rogers, N. (2005). Magma differentiation rates from (^{226}Ra/^{230}Th) and the size and power output of magma chambers. *Earth and Planetary Science Letters* **236**, 654–669.

Blundy, J. D. & Wood, B. J. (2003). Mineral–melt partitioning of uranium, thorium, and their daughters. In: Bourdon, B., Henderson, G. M., Lundstrom, C. C. & Turner, S. P. (eds) *U-series Geochemistry. Mineralogical Society of America and Geochemical Society, Reviews in Mineralogy and Geochemistry* **52**, 59–123.

Bourdon, B., Zindler, A. & Wörner, G. (1994). Evolution of the Laacher See magma chamber; evidence from SIMS and TIMS measurements of U/Th disequilibria in minerals and glasses. *Earth and Planetary Science Letters* **126**, 75–90.

Bourdon, B. & Sims, K. W. W. (2003). U-series constraints on intraplate basaltic magmatism. *Reviews in Mineralogy and Geochemistry* **52**, 215–254.

Bourdon, B., Turner, S. P. & Ribe, N. M. (2005). Partial melting and upwelling rates beneath the Azores from a U-series isotope perspective. *Earth and Planetary Science Letters* **239**, 42–56.

Brophy, J. G. (2008). A study of rare earth element (REE)–SiO$_2$ variations in felsic liquids generated by basalt fractionation and amphibolite melting: a potential test for discriminating between the two. *Contributions to Mineralogy and Petrology* **156**, 337–357.

Carracedo, J. C., Day, S. J., Guillou, H. & Gravestock, P. (1999). Later stages of volcanic evolution of La Palma, Canary Islands: rift evolution, giant landslides, and the genesis of the Caldera de Taburiente. *Geological Society of America Bulletin* **111**, 755–768.

Carracedo, J. C., Badiola, E. R., Guillou, H., de La Nuez, J. & Pérez Torrado, F. J. (2001). Geology and volcanology of La Palma and El Hierro, Western Canaries. *Estudios Geologicos* **57**, 175–273.

Claude-Ivanaj, C., Bourdon, B. & Allègre, C. J. (1998). Ra–Th–Sr isotope systematics in Grande Comore Island: a case study of plume–lithosphere interaction. *Earth and Planetary Science Letters* **164**, 99–117.

Davidson, J., Turner, S. & Plank, T. (2013). Dy/Dy*: variations arising from mantle sources and petrogenetic processes. *Journal of Petrology* **54**, 525–538.

Day, J. M. D., Pearson, D. G., Macpherson, C. G., Lowry, D. & Carracedo, J. C. (2010). Evidence for distinct proportions of subducted oceanic crust and lithosphere in HIMU-type

mantle beneath El Hierro and La Palma, Canary Islands. *Geochimica et Cosmochimica Acta* **74**, 6565–6589.

Dosseto, A., Turner, S. P., Sandiford, M. & Davidson, J. (2008). Uranium-series isotope and thermal constraints on the rate and depth of silicic magma genesis. In: Annen, C. & Zellmer, G. F. (eds) *Dynamics of Crustal Magma Transfer, Storage and Differentiation. Geological Society, London, Special Publications* **304**, 169–181.

Dosseto, A., Turner, S. & Van Orman, J. (2010). *Timescales of Magmatic Processes: from Core to Atmosphere*. Wiley–Blackwell, pp. 102–115.

Elkins, L. J., Sims, K. W. W., Prytulak, J., Blichert-Toft, J., Elliott, T., Blusztajn, J., Fretzdorff, S., Reagan, M., Hasse, K., Humphris, S. & Schilling, J. G. (2014). Melt generation beneath Arctic ridges: Implications from U decay series disequilibria in the Mohns, Knipovich, and Gakkel Ridges. *Geochimica et Cosmochimica Acta* **127**, 140–170.

Elliott, T. R. (1991). Element fractionation in the petrogenesis of ocean island basalts. PhD thesis, Open University, Milton Keynes, 192 pp.

Fisk, M. R., Upton, B. G. J. & Ford, C. E. (1988). Geochemical and experimental study of the genesis of magmas of Reunion Island, Indian Ocean. *Journal of Geophysical Research* **93**, 4933–4950.

Freestone, I. C. & Hamilton, D. L. (1980). The role of liquid immiscibility in the genesis of carbonatites—an experimental study. *Contributions to Mineralogy and Petrology* **73**, 105–117.

Garbe-Schönberg, C.-D. (1993). Simultaneous determination of thirty-seven trace elements in twenty-eight international rock standards by ICP-MS. *Geostandards Newsletter* **17**, 81–97.

George, R., Turner, S., Hawkesworth, C., Nye, C., Bacon, C., Stelling, P. & Dreher, S. (2004). Chemical versus temporal controls on the evolution of tholeiitic and calc-alkaline magmas at two volcanoes in the Aleutian arc. *Journal of Petrology* **45**, 203–219.

Ghiorso, M. S. & Sack, R. O. (1995). Chemical mass transfer in magmatic processes. IV A revised and internally consistent thermodynamic model for the interpretation and extrapolation of liquid–solid equilibria in magmatic systems at elevated temperatures and pressures. *Contributions to Mineralogy and Petrology* **119**, 197–212.

Gualda, G. A. R. & Ghiorso, M. S. (2014). MELTS_Excel: A Microsoft Excel-based MELTS interface for research and teaching of magma properties and evolution. *Geochemistry, Geophysics, Geosystems* http://dx.doi.org/10.1002/2014GC005545.

Guillou, H., Carracedo, J. C. & Day, S. (1998). Dating of the upper Pleistocene–Holocene activity of La Palma using the unspiked K–Ar technique. *Journal of Volcanology and Geothermal Research* **86**, 137–149.

Hart, S. R (1984). The DUPAL anomaly: a large scale isotopic anomaly in the southern hemisphere. *Nature* **309**, 753–756.

Hauri, E. H. & Hart, S. R. (1993). Re–Os isotope systematics of HIMU and EMII ocean island basalts from the South Pacific. *Earth and Planetary Science Letters* **114**, 353–371.

Hellman, P. L. & Green, T. H. (1979). The role of sphene as an accessory phase in the high-pressure partial melting of hydrous mafic compositions. *Earth and Planetary Science Letters* **42**, 191–201.

Hernandez-Pachero, A. & Valls, M. C. (1982). The historic eruptions of La Palma Island (Canarias). *Arquipelago, Reviews of the University of the Azores, Series C* **3**, 83–94.

Hernandez-Pachero, A. & De La Nuez, J. (1983). Las extrusiones salicas del Sur de la Isla de La Palma (Canarias). *Estudios Geologicos* **39**, 3–30.

Herzberg, C. & Asimow, P. D. (2008). Petrology of some oceanic island basalts: PRIMELT2.XLS software for primary magma calculation. *Geochemistry, Geophysics, Geosystems* Q09001.

Hoernle, K. & Tilton, G. (1991). Sr–Nd–Pb isotope data for Fuerteventura (Canary Islands) basal complex and subaerial volcanics: Applications to magma genesis and evolution. *Schweizerische Mineralogische und Petrographische Mitteilungen* **71**, 3–18.

Hoernle, K., Tilton, G. & Schmincke, H.-U. (1991). Sr–Nd–Pb isotopic evolution of Gran Canaria; evidence for shallow enriched mantle beneath the Canary Islands. *Earth and Planetary Science Letters* **106**, 44–64.

Hoernle, K., Tilton, G., Le Bas, M.J., Duggen, S. & Gerbe-Schonberg, D. (2002). Geochemistry of oceanic carbonatites compared with continental carbonatites: mantle recycling of oceanic crustal carbonate. *Contributions to Mineralogy and Petrology* **142**, 520–542.

Hoernle, K., Hauff, F., Kokfelt, T. F., Haase, K., Garbe-Schönberg, D. & Werner, R. (2011). On- and off-axis chemical heterogeneities along the South Atlantic Mid-Ocean-Ridge (5–11°S): Shallow or deep recycling of ocean crust and/or intraplate volcanism? *Earth and Planetary Science Letters* **306**, 86–97.

Hofmann, A. W. (1988). Chemical differentiation of the Earth: the relationship between mantle, continental and oceanic crust. *Earth and Planetary Science Letters* **90**, 297–314.

Hofmann, A. W., Jochum, K. P., Seufert, M. & White, W. M. (1986). Nb and Pb in oceanic basalts: new constraints on mantle evolution. *Earth and Planetary Science Letters* **79**, 33–45.

Imai, N., Terashima, S., Itoh, S. & Ando, A. (1995). 1994 Compilation of analytical data for minor and and trace elments in seventeen GSJ geochemical reference samples, 'igneous rock series'. *Geostandards Newsletter* **19**, 135–213.

Ionov, D. A. & Hofmann, A. W. (1995). Nb–Ta-rich mantle amphiboles and micas: implications for subduction-related metasomatic trace element fractionations. *Earth and Planetary Science Letters* **131**, 341–356.

Jacques, G., Hoernle, K., Gill, J., Hauff, F., Wehrmann, H., Garbe-Schonberg, D., van den Bogaard, P., Bindeman, I. & Lara, L. E. (2013). Across-arc geochemical variations in the Southern Volcanic Zone, Chile (34.5-38.0 °S): Constraints on mantle wedge and slab input compositions. *Geochimica et Cosmochimica Acta* **123**, 218–243.

Jochum, K. P., Nohl, U., Herwig, K., Lammel, E., Stoll, B. & Hofmann, A. W. (2005). GeoReM: a new geochemical database for reference materials and isotopic standards. *Geostandards and Geoanalytical Research* **29**, 333–338.

Johansen, T. S., Hauff, F., Hoernle, K., Klügel, A. & Kokfelt, T. F. (2005). Basanite to phonolite differentiation within 1550–1750 yr: U–Th–Ra isotopic evidence from the A.D. 1585 eruption on La Palma, Canary Islands. *Geology* **33**, 897–900.

Jones, H. J., Walker, D., Pickett, D. A., Murrell, M. T. & Beattie, P. (1995). Experimental investigations of the partitioning of Nb, Mo, Ba, Ce, Pb, Ra, Th, Pa, and U between immiscible carbonate and silicate liquids. *Geochimica et Cosmochimica Acta* **59**, 1307–1320.

Klügel, A., Hansteen, T. H. & Schmincke, H.-U. (1997). Rates of magma ascent and depths of magma reservoirs beneath La Palma (Canary Islands). *Terra Nova* **9**, 117–121.

Klügel, A., Hoernle, K. A., Schmincke, H.-U. & White, J. D. L. (2000). The chemically zoned 1949 eruption on La Palma (Canary Islands): petrologic evolution and magma supply dynamics of a rift zone eruption. *Journal of Geophysical Research* **105**, 5997–6016.

Klügel, A., Hansteen, T. H. & Galipp, K. (2005). Magma storage and underplating beneath Cumbre Vieja volcano, La Palma (Canary Islands). *Earth and Planetary Science Letters* **236**, 211–226.

Kogarko, L. N. (1997). Role of CO_2 on differentiation of ultramafic alkaline series: liquid immiscibility in carbonate-bearing phonolite dykes (Polar Siberia). *Mineralogical Magazine* **61**, 549–556.

Kokfelt, T. F., Hoernle, K. & Hauff, F. (2003). Upwelling and melting of the Iceland plume from radial variation of ^{238}U–^{230}Th disequilibria in postglacial volcanic rocks. *Earth and Planetary Science Letters* **214**, 167–186.

Kokfelt, T. F., Hoernle, K., Hauff, F., Fiebig, J., Werner, R. & Garbe-Schonberg, D. (2006). Combined trace element and Pb–Nd–Sr–O isotope evidence for recycled oceanic crust (upper and lower) in the Iceland mantle plume. *Journal of Petrology* **47**, 1705–1749.

Koornneef, J. M., Stracke, A., Bourdon, B. & Gronvold, K. (2012). The influence of source heterogeneity on the U–Th–Pa–Ra disequilibria in post-glacial tholeiites from Iceland. *Geochimica et Cosmochimica Acta* **87**, 243–266.

Latourrette, T., Hervig, R. L. & Holloway, J. R. (1995). Trace-element partitioning between amphibole, phlogopite and basanite melt. *Earth and Planetary Science Letters* **135**, 13–30.

Le Bas, M. J., Le Maitre, R. W., Streckeisen, A. & Zanettin, B. (1986). A chemical classification of volcanic rocks based on the total alkali–silica diagram. *Journal of Petrology* **27**, 745–750.

Luhr, J. F., Carmichael, I. S. E. & Varekamp, J. C. (1984). The 1982 eruptions of El Chichon volcano, Chiapas, Mexico: mineralogy and petrology of the anhydrite-bearing pumices. *Journal of Volcanology and Geothermal Research* **23**, 69–108.

Lundstrom, C. C., Hoernle, K. & Gill, J. (2003). U-series disequilibria in volcanic rocks from the Canary Islands: Plume versus lithospheric melting. *Geochimica et Cosmochimica Acta* **67**, 4153–4177.

Middlemost, E. A. K. (1972). Evolution of La Palma, Canary archipelago. *Contributions to Mineralogy and Petrology* **36**, 33–48.

Olin, P. H. & Wolff, J. A. (2012). Partitioning of rare earth and high field strength elements between titanite and phonolitic liquid. *Lithos* **128–131**, 46–54.

O'Neill, H. St. C. & Mallmann, G. (2007). The P/Nd ratio of basalts as an indicator of pyroxenite in its source. *Geochimica et Cosmochimica Acta* **71**, A741.

Praegel, N. O. & Holm, P. M. (2006). Lithospheric contributions to high-MgO basanites from the Cumbre Vieja Volcano, La Palma, Canary Islands and evidence for temporal variation in plume influence. *Journal of Volcanology and Geothermal Research* **149**, 213–239.

Prowatke, S. & Klemme, S. (2006). Trace element partitioning between apatite and silicate melts. *Geochimica et Cosmochimica Acta* **70**, 4513–4527.

Reagan, M. K., Turner, S., Legg, M., Sims, K. W. W. & Hards, V. L. (2008). ^{238}U- and ^{232}Th-decay series constraints on the timescales of crystal fractionation to produce the phonolite erupted in 2004 near Tristan da Cunha, South Atlantic Ocean. *Geochimica et Cosmochimica Acta* **72**, 4367–4378.

Rollinson, H. (1993). *Using Geochemical Data: Evaluation, Presentation, Interpretation*. Longman, 352 pp.

Schmitt, A. K., Wetzel, F., Cooper, K. M., Zou, H. & Wörner, G. (2010). Magmatic longevity of Laacher See volcano (Eifel, Germany) indicated by U–Th dating of intrusive carbonatites. *Journal of Petrology* **51**, 1053–1085.

Schwarz, S., Klügel, A., van den Bogaard, P. & Geldmacher, J. (2005). Internal structure and evolution of a volcanic rift system in the eastern North Atlantic: the Desertas rift zone, Madeira archipelago. *Journal of Volcanology and Geothermal Research* **14**, 123–155.

Sigmarsson, O., Condomines, M. & Ibarrola, E. (1992). ^{238}U–^{230}Th radioactive disequilibria in historic lavas from the Canary Islands and genetic implications. *Journal of Volcanology and Geothermal Research* **54**, 145–156.

Sigmarsson, O., Carn, S. & Carracedo, J. C. (1998). Systematics of U-series nuclides in primitive lavas from the 1730–36 eruption on Lanzarote, Canary Islands, and implications for the role of garnet pyroxenite during oceanic basalt formations. *Earth and Planetary Science Letters* **162**, 137–151.

Sims, K. W. W., Gill, J., Dosseto, A., Hoffmann, D. L., Lundstrom, C., Williams, R., Ball, L., Tollstrup, D., Turner, S., Prytulak, J., Glessner, J., Standish, J. & Elliott, T. (2008). An inter-laboratory assessment of the Th isotopic composition of synthetic and rock standards. *Geostandards and Geoanalytical Research* **32**, 65–91.

Sleep, N. H. (1990). Hotspots and mantle plumes: some phenomenology. *Journal of Geophysical Research* **95**, 6715–6736.

Stracke, A., Bourdon, B. & McKenzie, D. (2006). Melt extraction in the Earth's mantle: constraints from U–Th–Pa–Ra studies in oceanic basalts. *Earth and Planetary Science Letters* **244**, 97–112.

Thirlwall, M. F., Jenkins, C., Vroon, P. Z. & Mattey, D. P. (1997). Crustal interaction during construction of ocean islands: PbSrNdO isotope geochemistry of the shield basalts of Gran Canaria, Canary Islands. *Chemical Geology* **135**, 233–262.

Thomas, L. T., Hawkesworth, C. J., van Calsteren, P., Turner, S. P. & Rogers, N. W. (1999). Melt generation beneath ocean islands: a U–Th–Ra isotope study from Lanzarote in the Canary Islands. *Geochimica et Cosmochimica Acta* **63**, 4081–4099.

Turner, S. & Bourdon, B. (2010). Melt transport from the mantle to the crust—U-series isotopes. In: Dosseto, A., Turner, S. & Van Orman, J. (eds) *Timescales of Magmatic Processes: from Core to Atmosphere*. Wiley–Blackwell, pp. 102–115.

Turner, S., Evans, P. & Hawkesworth, C. (2001). Ultra-fast source-to-surface movement of melt at island arcs from ^{226}Ra–^{230}Th systematics. *Science* **292**, 1363–1366.

Turner, S., Sandiford, M., Reagan, M., Hawkesworth, C. & Hildreth, W. (2010). The origins of large volume, compositionally-zoned volcanic eruptions—new U-series isotope and numerical thermal modelling constraints on the 1912 Katmai–Novarupta eruption. *Journal of Geophysical Research* **115**, doi:10.1029/2009JB007195.

Turner, S., Kokfelt, T., Hauff, F., Hasse, K., Lundstrom, C., Hoernle, K., Yeo, I. & Devey, C. (2015). Mid-ocean ridge basalt generation along the slow-spreading, South Mid-Atlantic Ridge (5–11°S): inferences from ^{238}U–^{230}Th–^{226}Ra disequilibria. *Geochimica et Cosmochimica Acta* **169**, 152–166.

Watson, E. B. (1979). Apatite saturation in basic to intermediate magmas. *Contributions to Mineralogy and Petrology* **6**, 937–940.

Williams, R. W. & Gill, J. B. (1989). Effects of partial melting on the uranium decay series. *Geochimica et Cosmochimica Acta* **53**, 1607–1619.

Wörner, G., Beusen, J. M., Duchateau, N., Gijbels, R. & Schmincke, H.-U. (1983). Trace element abundances and mineral/melt distribution coefficients in phonolites from the Laacher See volcano (Germany). *Contributions to Mineralogy and Petrology* **84**, 152–173.

Yu, D., Fontignie, D. & Shilling, J.-G. (1997). Mantle plume-ridge interactions in the Central North Atlantic: A Nd isotope study of Mid-Atlantic Ridge basalts from 30°N to 50°N. *Earth and Planetary Science Letters* **146**, 259–272.

APPENDIX: DETERMINATION OF PARTITION COEFFICIENTS

For the determination of partition coefficients we analysed the rims of euhedral phenocrysts and the matrix (glass or groundmass) of suitable Cumbre Vieja samples for their trace element concentrations. The analyses were carried out on thin sections by laser ablation inductively coupled plasma mass spectrometry using a NewWave UP193ss solid-state laser coupled to a Thermo Element mass spectrometer at the Department of Geosciences, University of Bremen. Typical analytical conditions included a laser pulse rate of 5 Hz, irradiance of $\sim$1 GW cm^{-2}, spot size between 35 and 100 μm, helium ($\sim$0·8 l min^{-1}) as sample gas, argon ($\sim$0·8 l min^{-1}) as make-up gas, and a plasma power of 1200 W. Groundmass was analysed along traverses at a speed of 5 μm s^{-1}. The ThO/Th ratio determined on NIST612 glass was $\sim$0·1%. All isotopes were analysed at low resolution with five samples in a 20% mass window and a total dwell time of 25 ms per isotope; blanks were measured during 20 s prior to ablation. Great care was taken in scrutinizing the data to avoid mineral or melt inclusions. After every 5–12 data points either NIST610 or NIST612 glass was analysed as an external calibration standard. For data quantification Cetac GeoPro$^{™}$ software was used with Ca as internal standard. Analytical accuracy and precision were monitored by analyses of USGS glasses BCR2G and BHVO2G along with the samples; both are better than 10% for most elements. The full set of melt and mineral compositions and calculated partition coefficients are given in SD Electronic Appendix 3.